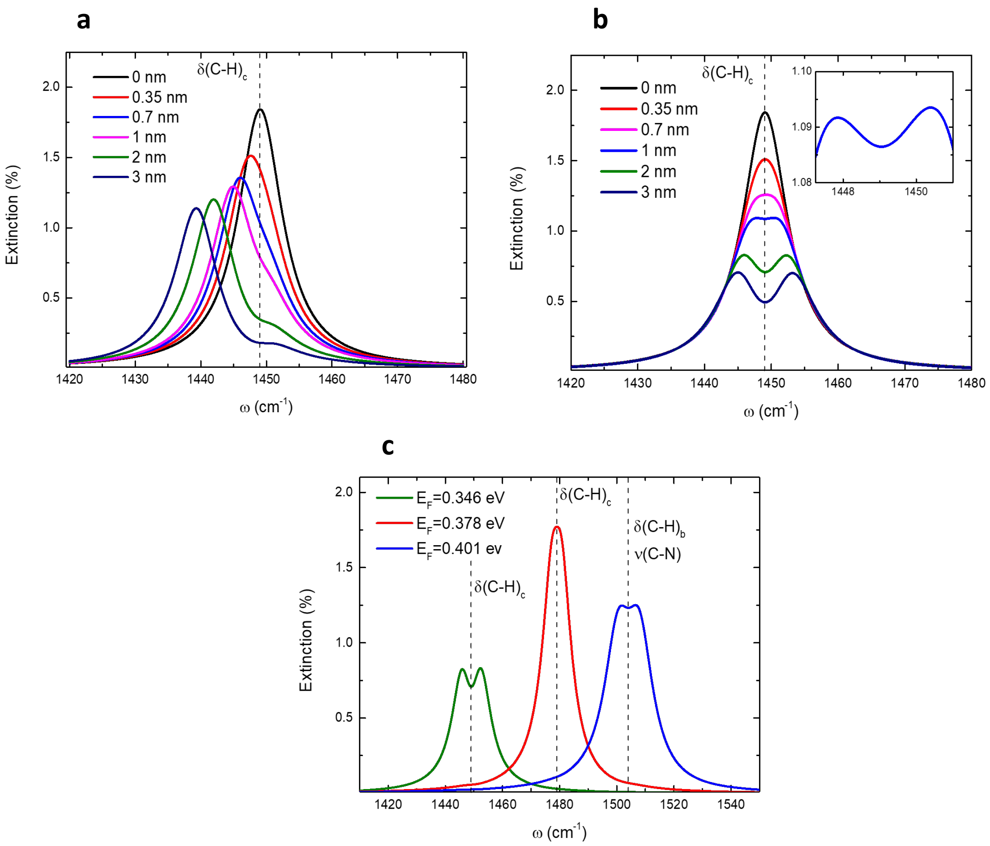

Figure 4.10: **a** Evolution of the extinction of the sensor for a CBP layer thickness ranging from 0 (no layer) up to 3 nm. The polariton wavevector is $k_p = 1.52 \times 10^7$ m^{-1} ($\lambda_{SAW} \approx 400$ nm) and the Fermi energy of the graphene layers at the top and bottom DLGs is set to $E_F = 0.339$ eV. **b** Evolution of the extinction of the sensor considering the same CBP thickness values as in (a) but adjusting the Fermi levels to compensate for the frequency shift ($k_p = 1.52 \times 10^7$ m^{-1} and $E_F = 0.339$, 0.341, 0.342, 0.343, 0.347 and 0.350 eV for CBP layer thickness ranging from 0 to 3 nm). The inset shows a magnified view of the 1 nm-thickness curve around the resonance frequency. **c** Extinction plots of the sensor covered by a 2 nm-thick CBP layer for $k_p = 1.52 \times 10^7$ m^{-1} and different E_F values to match the three resonances of CBP, as indicated by the black dashed lines.

(Kamenetskii et al., 2018). It usually receives the name of Fano resonance, and typically results from the interaction between a continuum of states and a discrete state (Kamenetskii et al., 2018). Therefore, its appearance depends not only on the strength of the interaction, but also on the relative difference between the linewidths of the vibrational resonance and that of the $SPPP_i$. Nevertheless, the interaction between the electric field of the polariton and the dipole associated with the molecular vibration is not always large enough to reach this regime, as can be seen in Figure 4.10(b) for a CBP thickness below 1 nm. The possibility of tuning the frequency response of the sensor not only allows to compensate for the frequency shift induced by the addition of the analyte layer but also to target different vibrational resonances with the same device. This is illustrated in Figure 4.10(c), where the Fermi energy is varied for a fixed CBP layer thickness in order to probe the distinct vibrational resonances that unambiguously fingerprint the analyte. This information can be complemented with the amount (thickness) of analyte being tested, obtained from the frequency shift of the extinction peak before any Fermi level correction is made. Furthermore, the SAW itself will also suffer from a frequency shift induced by the mass loading from the analyte, that can be detected monitoring the passband of the SAW device. Thus, these two signals can be used for autocalibration.

4.2 Coupled Oscillators Model

In the transparency-window regime of the sensor, the molecule-polariton interaction can be quantified by considering either the depth or the width of the transparency window. However, this cannot be applied to the broadening regime of the sensor, despite the molecule-polariton interaction is already strong enough to modify the spectrum, as seen in Figure 4.10(b). In order to continuously monitor the biosensor response, it is required to find a parameter suitable to quantify this interaction consistently across both regimes. Hence, it is necessary to fit the data from the TMM calculations to a distribution in order to find correlations between the fitting parameters and the amount of analyte being sensed. However, neither common peak distributions (Lorentzian, Gaussian, etc.) nor a combination of them (Voigt) are able to reproduce accurately the calculations in the transparency window regime. Since the transparency window arises from the coupling between two oscillating systems (the electric field of the polariton and the electric dipole of the vibrational transition), a Coupled Oscillators Model (COM) is proposed in which each of these systems is assumed to be a harmonic oscillator coupled to each other, both driven by an external force (the far-field light) and with a lifetime-dependent damping rate. The equations from Liu et al., 2009, adapted so both oscillators interact with light are:

$$\begin{aligned} \ddot{x}_1 + \gamma_1 \dot{x}_1 + \omega_1^2 x_1 + \kappa \dot{x}_2 &= F_1 \exp(-i\omega t) \\ \ddot{x}_2 + \gamma_2 \dot{x}_2 + \omega_2^2 x_2 - \kappa \dot{x}_1 &= F_2 \exp(-i\omega t) \end{aligned} \tag{4.1}$$

where $\mathrm{x_i}, \gamma_\mathrm{i}, \omega_\mathrm{i}$ and $\mathrm{F_i}$ are the amplitude, damping rate, resonance frequency, and driving force of each of the oscillators, and κ is the coupling parameter. Figure 4.11 shows a schematic of the coupled oscillators. The driving force of each individual oscillator, F_1 and F_2, can be understood as a measure of the direct interaction of each of them with the far-field light, while the coupling parameter κ accounts for the interaction (energy exchange) between them.

In order to solve these coupled differential equations, solutions of the type $\mathrm{x_i} = \mathrm{C_i e^{-i\omega t}}$ are assumed. Equation 4.1 can be then solved for $\mathrm{C_1}$ and $\mathrm{C_2}$, obtaining:

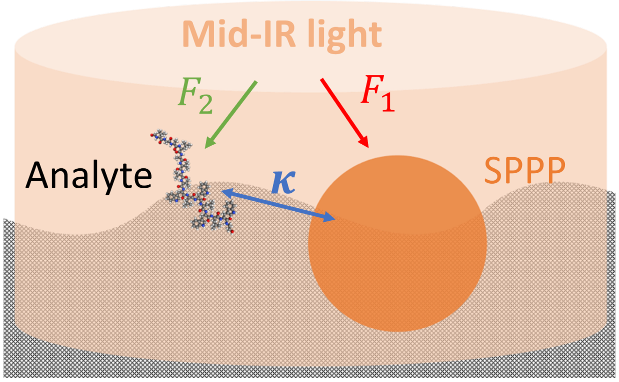

Figure 4.11: Schematic of the interactions considered for the coupled oscillators model.

$$
\begin{aligned}
C_1 &= \frac{(\omega_2^2 - i\omega\gamma_2 - \omega^2)F_1 + i\omega\kappa F_2}{(\omega_1^2 - i\omega\gamma_1 - \omega^2)(\omega_2^2 - i\omega\gamma_2 - \omega^2) - \omega^2\kappa^2} \\
C_2 &= \frac{i\omega\kappa F_1 + (\omega_1^2 - i\omega\gamma_1 - \omega^2)F_2}{(\omega_1^2 - i\omega\gamma_1 - \omega^2)(\omega_2^2 - i\omega\gamma_2 - \omega^2) - \omega^2\kappa^2}
\end{aligned} \tag{4.2}
$$

In the TMM calculations, the extinction is defined as the difference in reflection without and with the SAW activated (i.e. without and with coupling far-field light to the SPPP) normalised by the reflection without SAW:

$$
Ext = \frac{R_0 - R}{R_0} = 1 - \frac{R}{R_0} \tag{4.3}
$$

In the calculations of both R and R_0 there will be direct absorption of far-field light by the vibrational resonance of the analyte (hereafter referred to as oscillator 2), so the extinction will be proportional to the power absorbed by the SPPP (oscillator 1):

$$
\begin{aligned}
\langle P_1(t)\rangle &= \frac{1}{T}\int_0^T Re[F_1(t)]Re[\dot{x}_1(t)]dt = \frac{1}{T}\int_0^T Re[F_1 exp(-i\omega t)]Re[-i\omega C_1 \exp{(-i\omega t)}] = \\
&= \frac{1}{T}\int_0^T F_1\omega\cos{(\omega t)}[-Re(C_1)\sin{(\omega t)} + Im(C_1)\cos{(\omega t)}] = ... = \frac{F_1\omega}{2}Im(C_1)
\end{aligned} \tag{4.4}
$$

Therefore, the function which will reproduce the extinction spectra is:

$$
P(\omega) = \frac{F_1\omega}{2}Im[\frac{(\omega_2^2 - i\omega\gamma_2 - \omega^2)F_1 + i\omega\kappa F_2}{(\omega_1^2 - i\omega\gamma_1 - \omega^2)(\omega_2^2 - i\omega\gamma_2 - \omega^2) - \omega^2\kappa^2}] \tag{4.5}
$$

Here, ω_1 and γ_1 can be extracted by characterising the extinction of the biosensor before covering it with analyte, being respectively the position and the full width at half maximum of the SPPP peak and ω_2 and γ_2 can be obtained for a certain compound from their IR absorption spectra, which can be usually found in the literature or in databases for most compounds. This leaves F_1, F_2, and κ as fitting parameters. F_i hold information about the absorption of far-field light by the vibrational resonance of the compound and the SPPP, while κ represents the energy transfer rate between the two oscillators, thus the more intense the interaction, the larger its value.

In order to compare the results of the COM with those from the TMM simulations, a simplified structure comprised of, from bottom to top, an AlN substrate, a SLG and a 2-nm-thick layer of CBP (CBP/SLG/AlN) has been considered. Moreover, to reduce the number of resonances involved in the process, only one of the vibrational resonances of CBP has been considered (ω_{CBP2}). This simplifies the analysis while maintaining all the physical mechanisms involved. Thus, the simplified structure retains 3 resonances: the optical phonon of AlN ω_{TO} at 669 cm^{-1}, the vibrational resonance of CBP ω_{CBP2} at 1479 cm^{-1}, and the graphene plasmon ω_{pl}, which follows the dispersion equation (Low and Avouris, 2014):

$$\omega_{pl}(k) = \sqrt{\frac{2\alpha E_F ck}{\hbar\varepsilon_{eff}}}, \tag{4.6}$$

where $\alpha \sim 1/137$ is the fine structure constant, $\mathrm{E_F}$ is the Fermi energy of the graphene layer, c is the speed of light in vacuum, $\varepsilon_{\mathrm{eff}} = \frac{\varepsilon_{\mathrm{s}}+1}{2}$ is the effective permittivity of the substrate and air and k is the wavevector. These three resonances define a COM matrix. The 3x3 Hamiltonian will have 3 eigenvalues (3 branches in the dispersion). Assuming there is no coupling between the CBP resonance and the AlN phonon because of their large difference in frequency, this matrix reads

$$M = \begin{pmatrix} \omega_{pl} & g_{ph} & g_{CBP} \\ g_{ph} & \omega_{TO} & 0 \\ g_{CBP} & 0 & \omega_{CBP_2} \end{pmatrix}, \tag{4.7}$$

where $\mathrm{g_{ph}}$ and $\mathrm{g_{CBP}}$ are the coupling coefficients between the graphene plasmon and the AlN phonon and the vibrational resonance of CBP, respectively. These coupling coefficients, which can be obtained from the energy difference between the resonances (Fandan et al., 2021), are related to the κ parameter from 4.1.

Figure 4.12(a) compares the results from the TMM and the COM, showing a very good agreement for the calculation of the dispersion, both predicting the anticrossing point between the vibrational resonance and the SPPP, which leads to an upper (U) and a middle (M) branch. The lower (L) branch, which is not shown in the figure, would appear just below the other anticrossing point between the plasmon and the AlN TO phonon.

Figure 4.12(b) displays the squared modulus of the components of the eigenvector associated to each of the eigenvalues (branches of the dispersion), $|\mathrm{X_i}|^2$, in Figure 4.12(a). The relative weights of each component represent the plasmonic-phononic-vibrational character of the

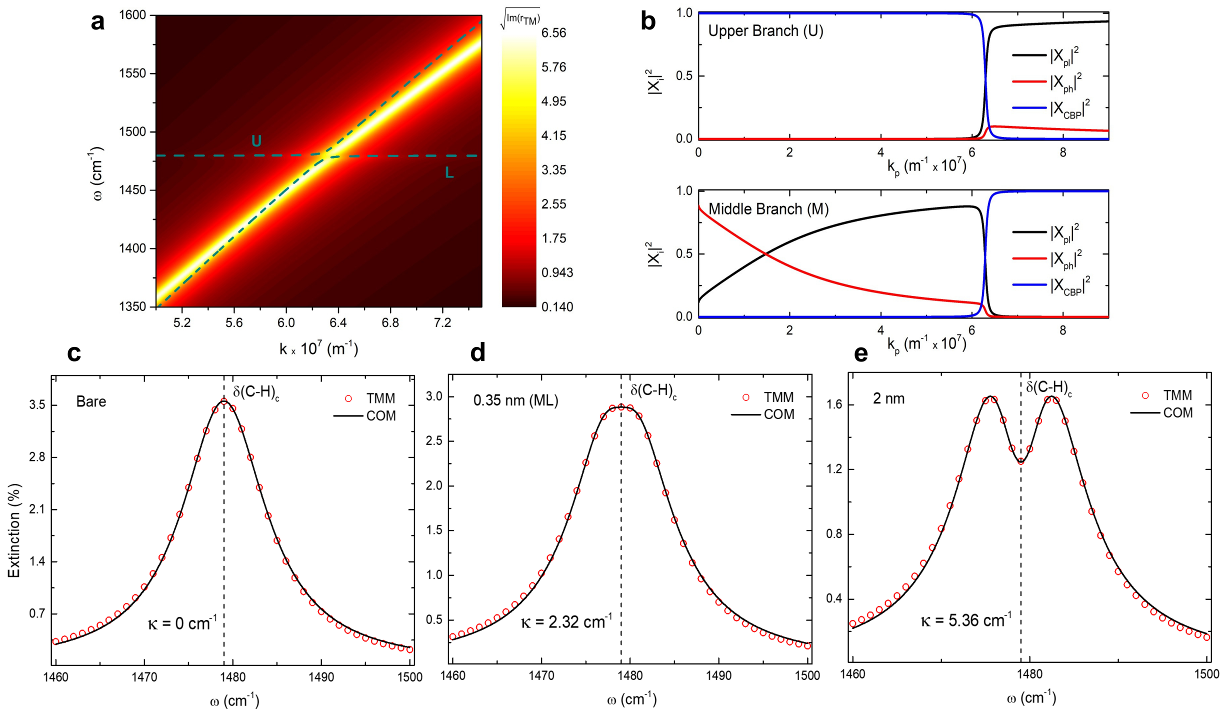

Figure 4.12: **a** Detail of the polariton dispersion of the CBP/SLG/AlN system around the vibration of the carbazole group of CBP (δ(C-H)$_c$ at 1479 cm^{-1}) calculated from the TMM (colorbar scale) and the COM (turquoise dashed lines) showing the upper (U) and middle (M) branches. **b** Eigenvectors of the COM Hamiltonian corresponding to each of the eigenvalues represented in (a). Different colours represent each of the components of the eigenvector, linked to the phononic/plasmonic/vibrational character of the polariton. In **c**, **d** and **e** the extinction of the CBP/SLG/AlN system calculated from the TMM (red circles) is plotted along with the COM model fitting function (black curves) for CBP thickness values of 0 nm (bare), 0.35 nm (1 ML) and 2 nm at a polariton wavevector $k_p = 6.29 \times 10^7$ m^{-1} ($\lambda_{SAW} \approx 100$ nm) and Fermi energies $\mathrm{E_F} = 0.376$, 0.381, and 0.403 eV, respectively. This large wavevector value is beyond the state-of-the-art resolution limit of an IDT, so examples in (c-e) are just to illustrate the simplified structure in (a) and (b). κ denotes the coupling coefficient between the polariton and the vibrational resonances extracted from equations 4.1 and 4.5.

polariton. These weights affect, for instance, the bandwidth of the polariton resonance, which will be given by the weighted sum of the bandwidths of the plasmon, the phonon, and the vibrational resonances. In terms of lifetimes, τ_i, this is expressed as

$$\frac{1}{\tau_p} = |X_{pl}|^2 \frac{1}{\tau_{pl}} + |X_{ph}|^2 \frac{1}{\tau_{ph}} + |X_{CBP}|^2 \frac{1}{\tau_{CBP}}. \tag{4.8}$$

The M branch is fully plasmonic-phononic until the vicinity of the anticrossing, where the vibrational resonance starts to hybridize with the SPPP. Conversely, the U branch has a pure vibrational nature for wavevectors below the anticrossing and hybridizes with the SPPP above it. It can be noted that the contribution of the phonon decreases with increasing wavevector in both M and U branches, as they move farther away from the energy of the phonon.

The derived power function of equation 4.5 can be used to fit the extinction curves calculated with the TMM. Figures 4.12(c)-(e) present the extinction curves of the CBP/SLG/AlN system calculated by the TMM (red dots) and their fitting to the COM (black curves) for different values of the CBP layer thickness. Both methods show a great agreement, not only when the interaction is strong enough to produce a transparency window within the peak, Figure 4.12(e), but also at weaker coupling, when the only noticeable effect is a broadening of the extinction peak, Figure 4.12(d). Furthermore, by using κ as a fitting parameter, the COM allows to extract quantitative information of the coupling even in the absence of a transparency window, thus permitting to monitor the interaction across different coupling regimes. Table A.1 in Annex A provides the values of the COM fitting parameters used in Figures 4.12(c-e).

The benefits of this model for the fingerprinting of organic compounds have been exemplified for CBP on a simple SLG/ALN system, but this methodology can be applied to other substances of biological interest such as thin layers of peptides or proteins on the full biosensor heterostructure, that is, the DLG/h-BN/DLG/AlN/Al/AlN system.

4.3 Fingerprinting Ultrathin Biolayers

The fitting method previously discussed has been used to study the sensing performance of the proposed biosensor with two different analytes, which are significant biological substances with weaker and broader resonances than CBP: a protein bilayer formed by the recombinant protein A/G and the goat anti-mouse immunoglobulin (IgG) (A/G-IgG) and monolayers of VGA peptide. The dielectric permittivities of these two materials have been calculated using the Kramers-Kronig relations (Lucarini et al., 2005) to compute the real part of the refractive index after extracting the imaginary part from absorption measurements in Rodrigo et al., 2015 (A/G-IgG) and Lavoie et al., 2002 (VGA), as described in Section 2.9.

4.3.1 A/G-IgG Protein Bilayer

A/G is a chimeric protein resulting from the complementary fusion of protein A and protein G, both of which hold immunoglobulin G (IgG) binding domains. This fusion retains the IgG binding domains from both proteins A and G, providing an improved binding receptor for IgG (Eliasson et al., 1988). Hence, this recombinant protein enhances the binding of goat anti-mouse IgG, that is, secondary antibodies generated by immunising goat specimens with mouse immunoglobulin, which are widely used in research as a primary antibody marking (Lin et al., 2016) or for antibody-based tumour therapy (Vukovic et al., 2023). As can be seen in the frequency-dependent permittivity curves shown in Figure 2.9, this protein bilayer presents 2 absorption bands around 1655 cm^{-1} and 1530 cm^{-1}, corresponding to the vibrational resonances of the amide I and amide II groups, respectively.

Figure 4.13 illustrates the biosensor response when coated with a 8-nm-thick A/G-IgG protein bilayer. This bilayer has been reported to be formed by incubation of A/G, which forms a monolayer through physisorption, followed by rinsing in PBST to eliminate excess protein, and then incubation in IgG, which binds to the previously attached A/G monolayer (Rodrigo et al., 2015).

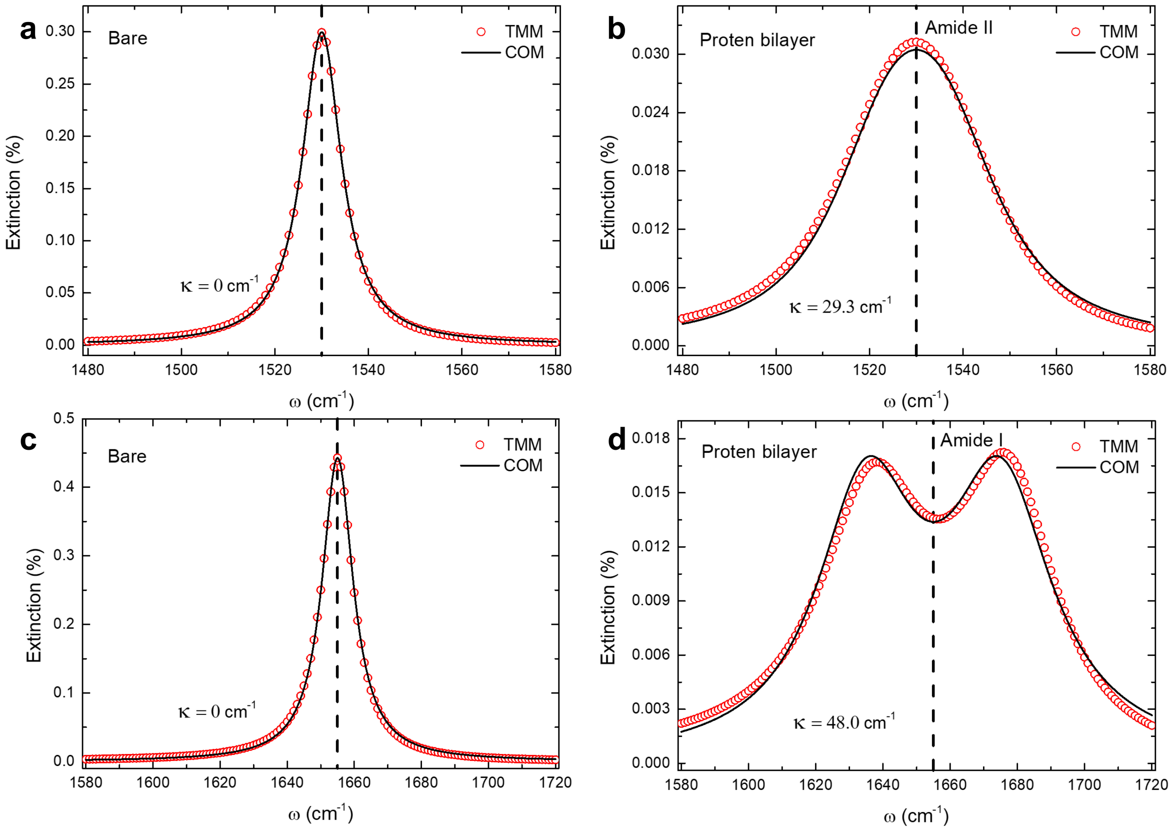

Figure 4.13: Response of the biosensor to an A/G-IgG protein bilayer calculated by the TMM (red circles) and the COM (black curve). The comparison of the extinction of the DLG/h-BN/DLG/AlN/Al/AlN heterostructure **a**,**c** uncoated and **b**,**d** coated with the A/G-IgG protein bilayer indicates the capability of the sensor to fingerprint the protein through its amide I and II bands. The coupling coefficient κ between the polariton and the vibrational resonance is indicated in each case. The polariton wavevector is $k_p = 1.7 \times 10^7$ m^{-1} ($\lambda_{SAW} \approx 360$ nm) in (a) and (b) and 2.1×10^7 m^{-1} ($\lambda_{SAW} \approx 300$ nm) in (c) and (d), whereas the Fermi energy is tuned to $E_F = 0.371$, 0.386, 0.373, and 0.396 eV in (a, b, c, d), respectively, in order match the frequency of the polariton with those of the amide bands.

When the protein bilayer is deposited on the device, there is a frequency shift in the SPPP resonance due to the change in the dielectric environment, that can be balanced by gate doping to make the SPPP peak overlap that of the amide group to be sensed. In the case of amide II, a considerable broadening is observed in the SPPP peak when it is tuned to the frequency of the amide II band, as observed comparing the SPPP in the bare sensor, Figure 4.13(a) (κ=0), and the SPPP interacting with the resonance of the amide II group in the coated sensor, Figure 4.13(b) (κ=29.3 cm^{-1}). In contrast, for the amide I band, a transparency window appears within the peak, centred at 1655 cm^{-1}, resulting from a stronger polariton-protein interaction. This is clearly observed when comparing the SPPP in the bare sensor, Figure 4.13(c) (κ=0), and the SPPP interacting with the resonance of the amide I group in the coated sensor, Figure 4.13(d) (κ=48 cm^{-1}).

Therefore, by fitting to the COM model, the coupling between the vibrational fingerprint and the polariton can be quantified in all cases, allowing to distinguish whether the protein bilayer is present, even in the absence of a transparency window. In this latter case, the presence of the analyte is detected qualitatively as an increase in the width of the extinction peak and quantitatively as a prominent variation of the κ parameter. It has to be noted that, although the κ parameter has much higher values in the A/G-IgG protein bilayer for both amide groups, as compared to those of the carbazole group of CBP $\delta(\mathrm{C-H})_\mathrm{c}$ (see Figures 4.13(d,e)), the transparency window only appears in the amide I region and not in the amide II. This is because the coupling is not only governed by the rate of energy exchange between oscillators (κ parameter), but also by the relation of this exchange rate and the decay rates of the oscillators (their damping coefficients γ_i). Therefore, since the amide bands are wider (i.e. have larger γ_i) than the vibrational resonances of CBP, a higher κ value is needed to observe a crossover from the initial broadening regime to the subsequent transparency-window regime. The values of the parameters extracted from the COM fitting are provided in Table A.1 in Appendix A.

4.3.2 Valine Gramicidin A Peptide Monolayer(s)

Gramicidin is a polypeptide discovered in 1939 that, along with tyrothricin, is considered the first antibiotic agent clinically tested (Dubos and Hotchkiss, 1941; Epps, 2006). It is composed by 15 hydrophobic aminoacids following the sequence formyl-L-X-gly-L-ala-D-leu-L-ala-D-val-L-val-D-val-L-trp-D-leu-L-Y-D-leu-L-trp-D-leu-L-trp-ethanolamine, where X can be valine or isoleucine and, depending on the aminoacid Y being tryptophan, phenylalanine, or tyrosine, the compound will be called gramicidin A, B or C. Furthermore, Lavoie et al., 2002 demonstrated that VGA can be obtained as a monolayer following the Langmuir-Blodgett method. Because of the importance of VGA as an antibiotic substance, it was chosen as an analyte to be studied with the biosensor designed. Therefore, the biosensor operation has been simulated after different numbers of VGA monolayers were transferred, and the variations of the signal when the amount of analyte is changed are explored. As seen in Figure 2.9, VGA presents its Amide I and Amide II bands at 1637 cm^{-1} and 1452 cm^{-1}, respectively.

Figure 4.14 present the biosensor response in the amide I region when coated with up to three VGA peptide MLs. The extinction spectra show how the SPPP peak broadens gradually as the thickness of VGA is increased up to 2 MLs, whereas a Fano resonance develops for 3 MLs. Again, the COM allows us to quantify the amount of peptide in all cases, confirming that the initial broadening originates from the interaction between the SPPP electric field and the vibrational electric dipole, that later evolves into a transparency window. In all the previous spectra, the frequency shift in the SPPP resonance due to the change in the dielectric environment has been counteracted by gate doping to force the SPPP peak overlap that of the amide I group. Figure 4.15(a) shows this frequency shift, that could also be used to quantify the amount of analyte deposited on top of the sensor. In order to assess the sensitivity of the sensor, Figure 4.15(b) depicts the difference in reflectance calculated for the

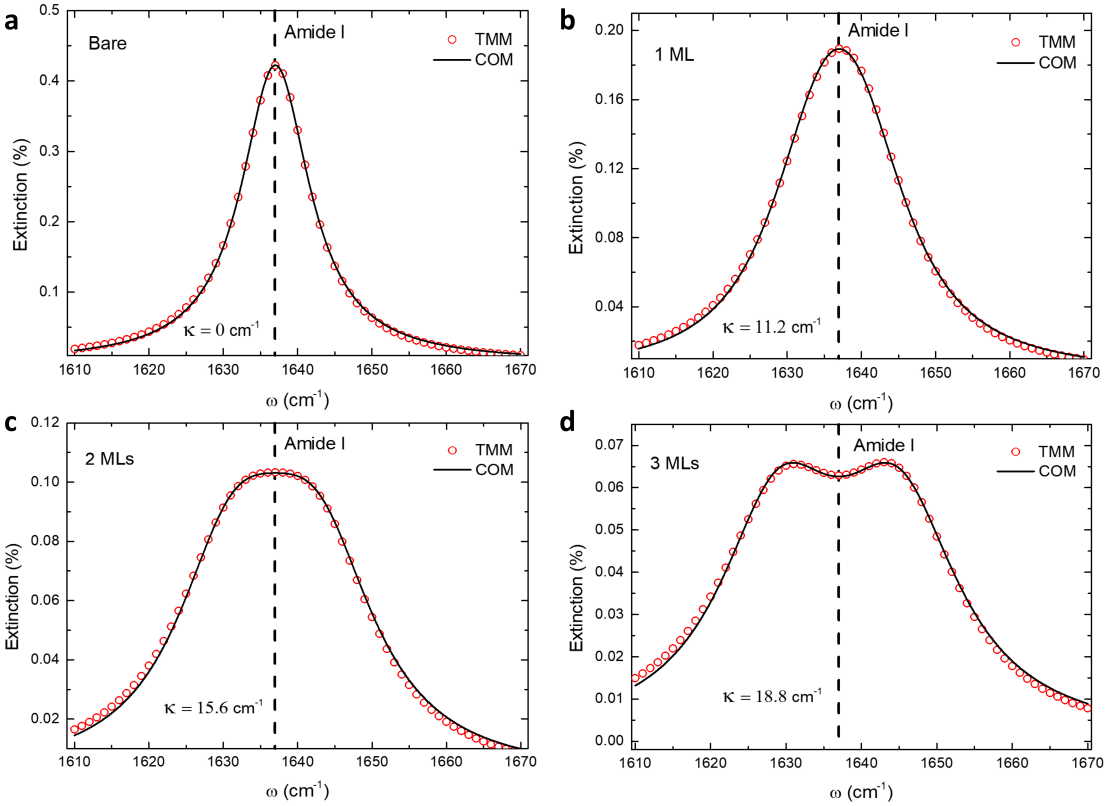

Figure 4.14: Response of the biosensor to 1-3 MLs of VGA peptide calculated by the TMM (red circles) and the COM (black curve). The comparison of the extinction of the DLG/h-BN/DLG/AlN/Al/AlN heterostructure **a** uncoated and coated with **b** 1, **c** 2, and **d** 3 MLs of VGA indicates the capability of the sensor to distinguish the three cases unambiguously. In each case, the coupling coefficient κ between the polariton and the vibrational resonance is indicated. The polariton wavevector is $k_p = 2 \times 10^7$ m^{-1} ($\lambda_{SAW} \approx 300$ nm), whereas the Fermi energy is tuned to $E_F = 0.381$, 0.396, 0.410, and 0.423 eV for the bare sensor and the sensor covered by 1, 2, and 3 MLs of VGA, respectively, in order match the frequency of the polariton with that of the amide I band.

DLG/h-BN/DLG/AlN/Al/AlN heterostructure coated with an increasing number of VGA MLs as compared to that provided by those MLs on a bare AlN substrate without polaritons. It can be pointed out that the polariton enhances the detection signal by approximately 16 times in the ML limit and by 4 times for the 2-ML case. This provides a powerful tool for assessing VGA, both as a monolayer and a bilayer, the latter being specially interesting as it forms ion channels that allow conduction of monovalent cations through lipid membranes. The values of the parameters extracted from the COM fitting are provided in Table A.1 in Annex A.

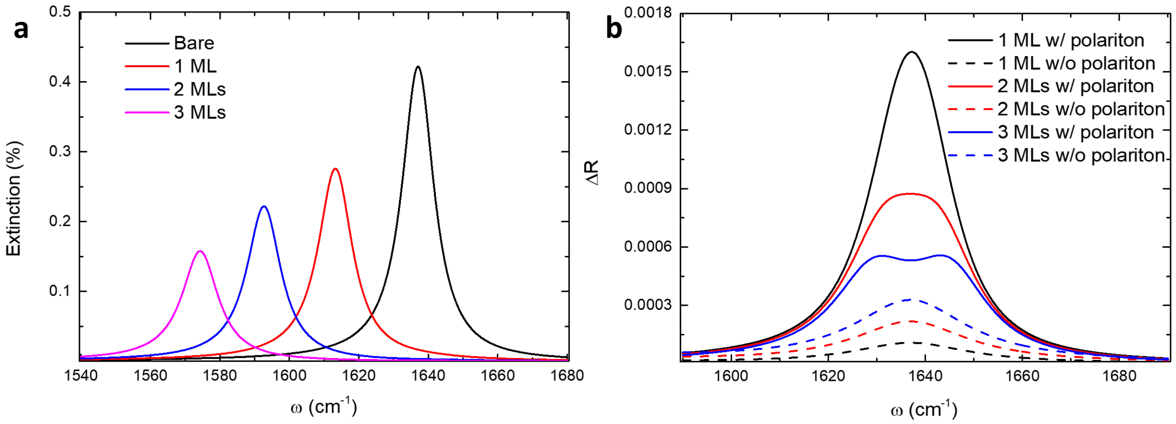

Figure 4.15: **a** Frequency shift in the biosensor response due to the change in the dielectric environment produced by up to 3 MLs of VGA deposited on the sensor surface at a fixed $E_F = 0.381$ eV value. Note that, for fingerprinting, the Fermi level of graphene must be tuned as in 4.14(b-d), though this shift can be used for quantifying the amount of analyte. **b** Comparison of the change in reflectance ΔR produced in the DLG/h-BN/DLG/AlN/Al/AlN heterostructure (i.e. with polariton) vs in a bare AlN substrate (i.e. without polariton), when both are coated with up to 3 MLs of VGA.

4.4 Influence of Graphene Quality on Biosensor Performance

For these calculations, a graphene mobility of $\mu = 10000$ cm^2 V^{-1}s^{-1} has been assumed, which is an intermediate value between those for graphene single crystals encapsulated in h-BN (of the order of $\mu = 70000$ cm^2 V^{-1}s^{-1}, see, for example, Fazio et al., 2019) and those from commercial polycristalline graphene (of around $\mu = 1500$ cm^2 V^{-1}s^{-1}, see for example Graphenea, Last accessed 2024). In order to shown the effect of the mobility on the biosensor performance, Figure 4.16 shows the spectrum from Figure 4.13(d) calculated using different values for the carrier mobility. By decreasing the mobility from $\mu = 10000$ cm^2 V^{-1}s^{-1} to values as low as $\mu = 1500$ cm^2 V^{-1}s^{-1}, a significant drop in the extinction is observed, although the Fano interference pattern remains visible in all cases. Nevertheless, it has to be noted that the proposed biosensor is able to operate normally even in the abscence of a Fano resonance. Conversely, higher mobility values lead to an increment in the extinction, as it effectively increases the conductivity of graphene, reaching a 50% enhancement in the Fano resonance depth for a mobility $\mu = 40000$ cm^2 V^{-1}s^{-1} as compared to $\mu = 10000$ cm^2 V^{-1}s^{-1}. The carrier mobility value takes into account different mechanisms that contribute to define the electron lifetime, such as crystal defects or grain boundaries in graphene, as well as polymer residues from the transfer process. Thus, by reducing these sources of scattering with higher quality graphene or post-transfer cleaning processes (Tyagi et al., 2022; Rasouli et al., 2023), the signal of the biosensor can be significantly increased.

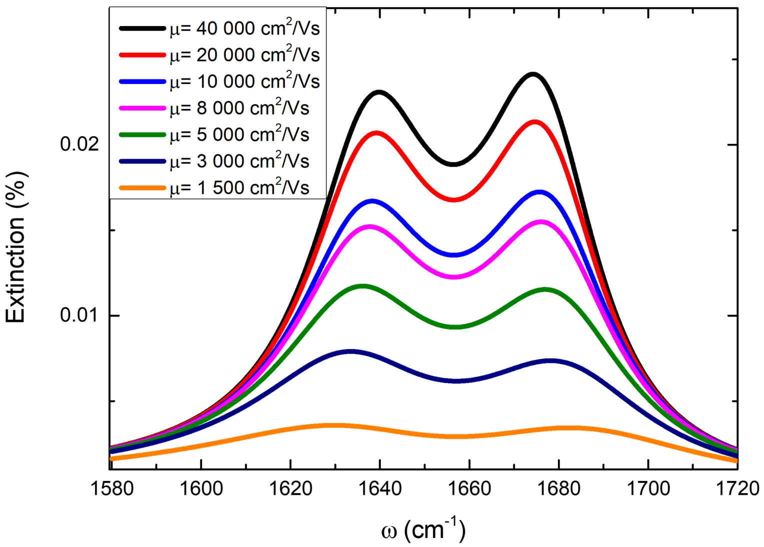

Figure 4.16: Response of the biosensor to an A/G-IgG protein bilayer calculated by the TMM for different values of the electron mobility of graphene, which represents different density of imperfections (more defects lead to lower electron mobility values).

4.5 Comparison of tailored SPPP in the biosensor heterostructure with surface plasmon and surface phonon polaritons in other materials

The quality factor (Q) of an electrostatic mode is a function of the resonant wavelength, but is independent of the details of the geometry by which this resonance is realized (Wang and Shen, 2006). Moreover, it can be estimated directly from the optical constants. Therefore, Caldwell et al., 2015 have used it as a wavelength-dependent figure of merit (FOM) to compare a broad range of materials supporting both surface phonon and surface plasmon polaritons.

The Q factor, calculated as the ratio between the centre frequency ω_p and the bandwidth $\Delta\omega$ of the resonance, contains information about the capacity of the resonator to store energy. In addition, according to Caldwell et al., 2015, the Q factor is also related to the spatial confinement of the polariton mode through

$$Q = \frac{\omega_p}{\Delta\omega} \approx \frac{L_p}{2L_m}, \tag{4.9}$$

where L_p and L_m are, respectively, the propagation length and vertical extent of the polariton. In this equation, it has been assumed a long wavelength limit and the damping rate of the resonance being equal to its full width at half maximum.

Figure 4.17 shows the Q factor as a function of the wavelength for the SPPP in the DLG/h-BN/DLG/AlN/Al/AlN heterostructure used in the proposed biosensor in comparison with the plasmonic and phononic polaritons in other material systems, including metals, alloyed metals, doped semiconductors, and polar dielectrics (Caldwell et al., 2015). In the case of the SPPP, a biosensor with $\lambda_{SAW} = 310$ nm has been simulated with different values of the Fermi level that allow to scan the 1450-1700 cm^{-1} frequency range. It can be noted that the reported SPPP in the DLG/h-BN/DLG/AlN/Al/AlN heterostructure present a very high Q factor, comparable to that of plasmons in gold and above polaritons in all other materials except for surface plasmon polaritons in silver and aluminum and surface phonon polaritons in 4H-SiC. Moreover, the electrostatic modulation of the Fermi level of graphene in the biosensor heterostructure provides the unique capability of tuning the polariton frequency, that no other material in the figure holds, and that permits to cover the whole frequency range required for the fingerprinting of significant biomolecules, such as proteins.

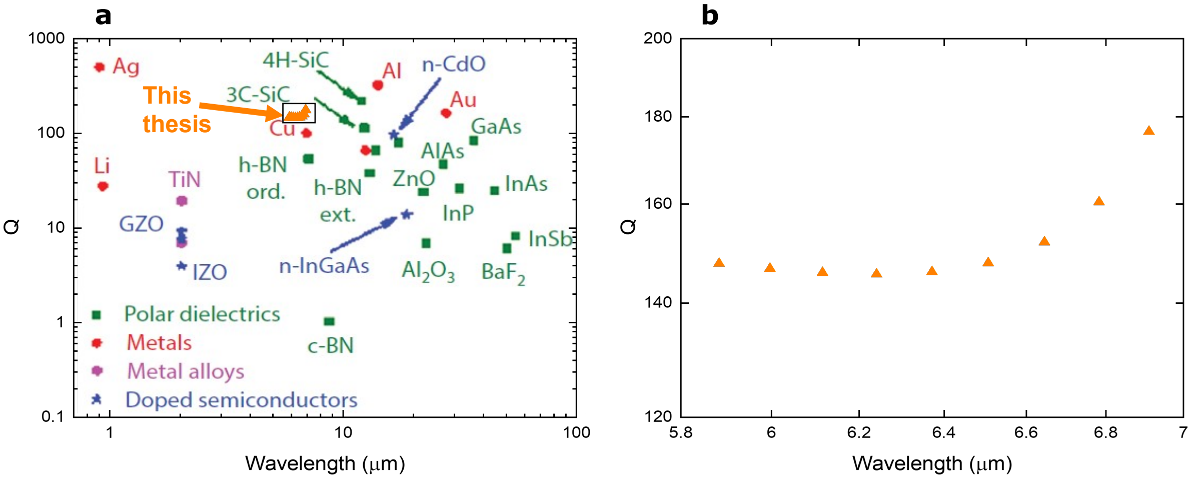

Figure 4.17: **a** Comparison of the Q factor of the SPPP in the DLG/h-BN/DLG/AlN/Al/AlN heterostructure of the designed biosensor (orange triangles) with the surface plasmon and surface phonon polaritons in other materials considered in Caldwell et al., 2015. **b** Magnified view of (a) in the operation frequency range of the biosensor.

For example, as a comparison, Figure 4.18(a) shows the dispersion of an h-BN/AlN structure, where graphene has been removed and the h-BN layer thickness has been increased up to 80 nm so intense phonon polaritons emerge. In such a device without graphene, there is no way to dynamically modulate the frequencies of the polaritons in the fingerprint region, since they will be fixed by the thickness of h-BN and the SAW wavelength. Moreover, as seen in Figure 4.18(b), the maximum frequency that can be accessed using SAWs as a coupling mechanism is 1560 cm^{-1} , which is not sufficient for allow this device to probing the Amide I band of proteins and peptides.

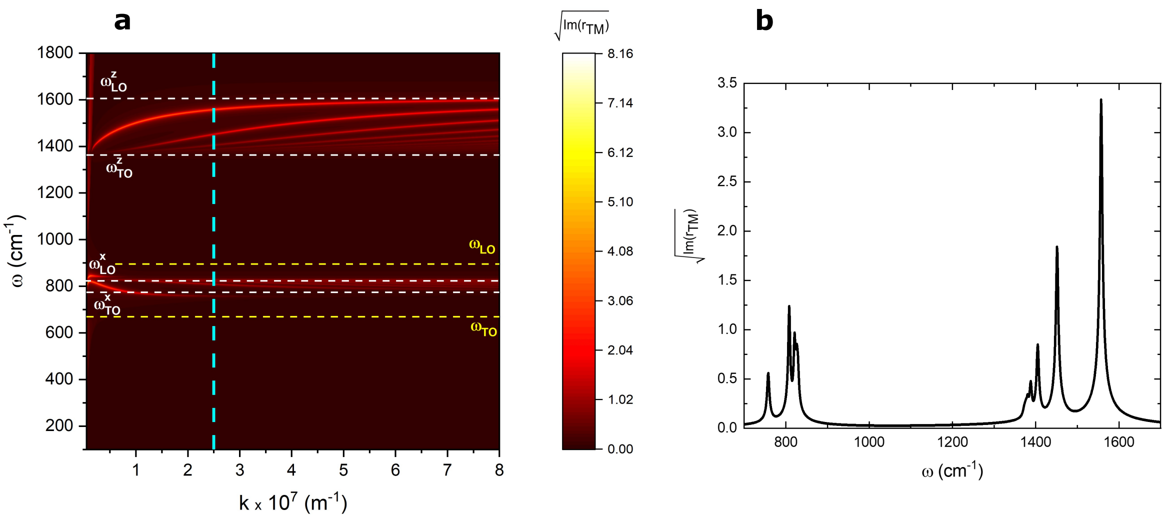

Figure 4.18: **a** Dispersion of phonon polaritons in a h-BN/AlN/Al/AlN system where the thickness of h-BN is 80 nm. **b** Cross section of (a) at k = 2.5×10^7 m^-1, corresponding with $\lambda_{SAW} = 250$ nm.

Chapter 5

QCL Setup for Mid-IR Spectroscopy and Mapping

With aims to study mid-IR plasmons in graphene, especially those induced by SAWs, as described in the previous chapter, a spectroscopy and mapping setup working in this spectral range has been assembled. The different options considered, especially for the choice of source and detector and the design of the optical path, as well as the required calibrations, are discussed in this chapter.

The standard technique for mid-IR analysis is FTIR spectroscopy. In this technique, a globar, a thermal emitter of infrared radiation, is used in combination with an interferometer to record spectral data. Since the emitter is a thermal source, it provides a broad spectral range to work in, at the expense of a reduced emitted power at each specific wavelength. Despite this reduction of power results in a low signal, the thermal source experiences little power fluctuations, thus the measurement noise is just limited by the detector. This results in high signal-to-noise ratios (Schwaighofer et al., 2018), although it faces limitations when measuring in the presence of water, either in liquid or in vapour phase, due to its strong absorption lines in this range.

Conversely, a laser provides a higher optical power, which not only helps to overcome the water absorption issue, but also increases the detected signal level. However, the variety of laser sources that can emit in the range of the amide bands discussed in the previous chapter is reduced. Moreover, the wavenumber tuning range of sources in this range as the CO_2 laser or the distributed feedback (DFB) semiconductor lasers is very limited. Quantum cascade lasers (QCLs) are laser sources based on intersubband transitions in semiconductor quantum wells. Currently available QCLs allow laser emission in the 3-14 μm range, with output peak powers of several Watts and spectral accuracy as good as 2 cm^{-1} ("Alpes Lasers", Last accessed 2024; "Block Engineering", Last accessed 2024; "Daylight Solutions", Last accessed 2024; "Sacher Lasertechnik", Last accessed 2024). Moreover, there are broad gain QCLs that allow emission in a wide wavenumber range of up to hundreds of cm^{-1}. In addition, external cavity QCLs combine the broad gain spectra of these QCLs with the wavelength filtering of a diffraction grating, thus providing narrow linewidth emission in a wide spectral range.

Furthermore, QCLs are linearly polarised and coherent sources, enabling interferometric or polarisation-based (such as vibrational circular dichroism) measurement schemes (Hayden et al., 2018; Hermann et al., 2022). In addition, a QCL-based system has the capability to measure continuously at a single wavelength instead of recording spectra, allowing for efficient monitoring, fast mapping, or time-resolved measurements.

Several studies have been conducted on the suitability of QCLs or FTIR for mid-IR measurements (Isensee et al., 2018; Schwaighofer et al., 2018). In gaseous measurements, the absorption of water vapour is low, but so is the absorption of the compounds of interest, especially at very low concentrations. In a liquid environment, Schwaighofer et al., 2018 shows that the higher power of QCLs allows larger optical paths than those that can be measured by FTIR spectroscopy due to water absorption, increasing the signal and facilitating sample handling. Moreover, this study proposes a signal processing protocol that results in signal-to-noise ratios almost twice as large as those achieved by FTIR spectroscopy in fast measurements, although in a narrower spectral range. The spectral range of a QCL depends on the techonology employed for the wavelength selection. Hence, distributed feedback QCLs (DFB QCLs) count with an on-chip fixed diffraction grating that locks the resulting optical mode. In DFB QCLs, the emission range is thus limited to that enabled by changes in temperature, which is a slow process. On the other hand, in external cavity QCLs (EC-QCLs), the diffraction grating that selects the emission wavelength is not physically attached to the QCL chip, so it is possible to rotate it mechanically, increasing both the tunability range and the scanning speed of the emitter.

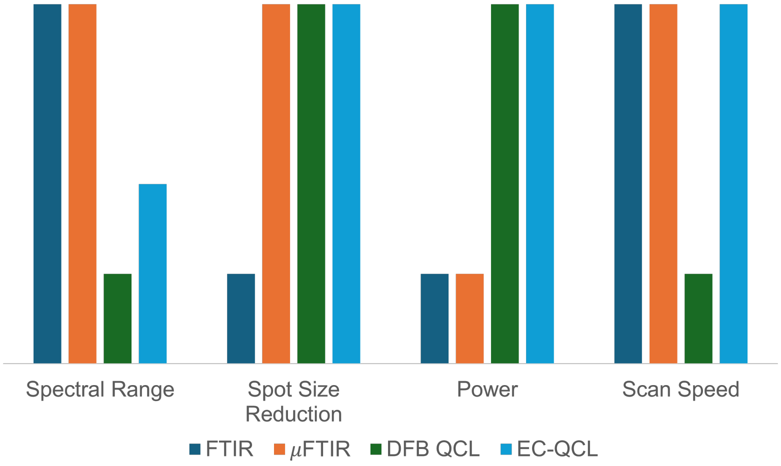

Figure 5.1: Graphical comparison of QCL and FTIR spectroscopy.

One of the goals of the spectroscopy setup devised in this chapter is to enable the detection of SAW-driven SPPs. For that, mid-IR radiation needs to be focused in the beam path of the SAW, where the size of the wavefront scales with the SAW wavelength. In Chapter 3, the devices with a wavelength of 1.6 μm had an IDT aperture of $\sim 60\mu$m. However, according to the calculations in Chapter 4, SAW devices with wavelength values of hundreds of nanometres are needed, so smaller apertures are foreseen. Therefore, radiation needs to be focussed to a small spot size with a sufficiently high power density. Although conventional FTIR spectroscopy systems are limited in this regard, FTIR microscopy systems ("Bruker Guide to FTIR Microsocopy", Last accessed 2024) can overcome this difficulty. However, in the case of SAW-driven SPPs, small signals are expected, and thus a high initial optical power is preferred. Hence, EC-QCLs have been chosen as mid-IR sources for the spectroscopy setup. Figure 5.1 shows a summary of the comparison between QCL and FTIR spectroscopy regarding the main features discussed: spectral width, spot size, power and frequency scan speed.

Some companies offer already complete spectroscopy systems, with emitter, detector, and measuring software, such as the LaserScope by Block Engineering ("LaserScope by Block Engineering", Last accessed 2024, discontinued) or the Spero IR Microscope by Daylight Solutions ("Spero IR by Daylight Solutions", Last accessed 2024). Moreover, these systems, as others like the MIRcat by Daylight Solutions ("MIRcat by Daylight Solutions", Last accessed 2024), offer up to four different QCL chips in a single system, thus providing a broad, continuous emission range while also vastly simplifying the optical setup. Some of the commercial systems mentioned are shown in Figure 5.2. While these closed systems are ready to be used, building the system by choosing its different components allows one to have a more flexible spectroscopy setup suited to the particular needs of the research, such as having the optimal emitters and detectors for the desired range, as well as a versatile control software. The cost of the system was also a limiting factor, and the choice of the product and its functionalities needed to be adjusted to the budget; thus, commercial all-in-one systems were dismissed in favour of open, customisable, and cost-efficient options.

5.1 External Cavity Quantum Cascade Lasers

After reviewing the commercially available light sources, external cavity QCLs have been chosen for the spectroscopy setup, as they provide a higher output power as compared to a globar, while maintaining a narrow linewidth and a high tunable range. This is key for on-chip plasmonic devices such as the SAW-driven SPPPs discussed in the previous chapter, since a higher radiation power needs to be addressed to small areas with a lateral size of tens of μm. In particular, two broad gain QCLs with an external cavity have been incorporated in the setup: BG-6.1-7.4 and BG-10.8-13.7 from Alpes Lasers, both in combination with the Alpes Lasers's external cavity laser kit. The laser spectra provided by the manufacturer are shown in Figure 5.3.

Even though the combination of these two lasers does not offer a continuous emission range, these lasers were picked because five out of six phonon lines of AlN and h-BN fall in their emission range, allowing to use them to excite SPPPs with the heterostructure discussed in chapter 4. Moreover, both the Amide I and Amide II bands are also located within the highest part of the energy spectrum of the QCLs, as can be seen in Figure 5.3. Thus, they are suitable for fingerprinting organic compounds.

Each laser chip has an integrated front mirror and is attached to a copper heatsink with a Peltier cooling system, while a diffraction grating in Littrow's configuration (Duarte, 1995), set on a motorised rotary mount, plays the role of both the backside reflector and the spectral

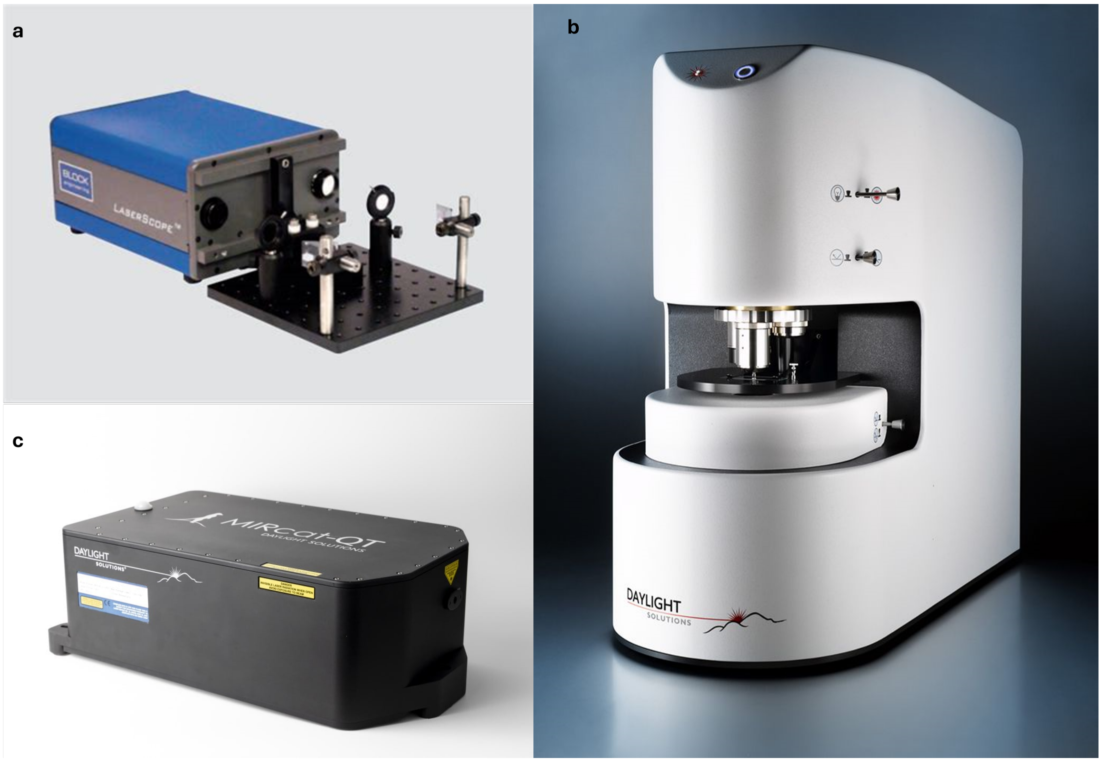

Figure 5.2: Commercial systems for mid IR spectroscopy. **a** Block Engineering's LaserScope ("LaserScope by Block Engineering", Last accessed 2024, discontinued), **b** Spero IR Microscope ("Spero IR by Daylight Solutions", Last accessed 2024) and **c** Mircat by Daylight Solutions ("MIRcat by Daylight Solutions", Last accessed 2024).

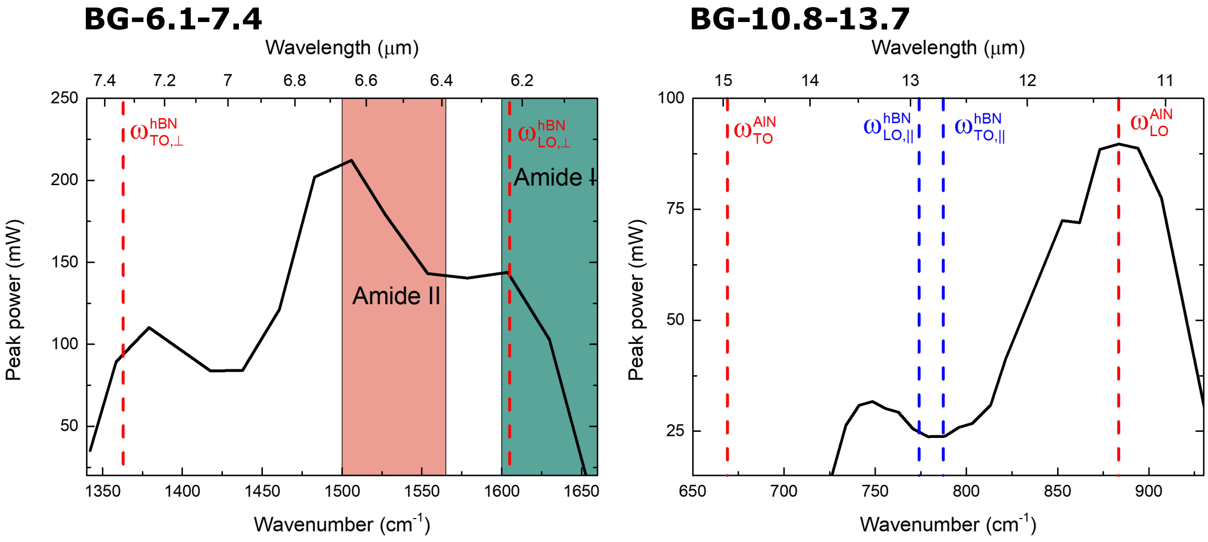

Figure 5.3: QCL spectra as provided by the manufacturer. The phonon lines of AlN and hBN are indicated by the vertical dashed lines and the approximate position of the amide bands is displayed as coloured regions.

filter in the cavity, as shown in Figure 5.4. Therefore, the angle between the grating and the incoming beam can be electrically controlled, and since different wavelengths reflect on the grating at different angles, this results in a way of electrically controlling the wavelength that is allowed in the cavity, and thus the emitted wavelength.

As for the pumping mechanism, the laser is electrically driven by an S-2 pulser from Alpes Lasers, which delivers 250-300 ns pulses to the lasers. It is possible to extract the pulse signal to use it as a reference signal in lock-in measurements. Figure 5.5 shows both the reference pulse from the S-2 pulser and the laser pulse measured at the photodetector. All the electrical components of the laser (grating driving stage, thermoelectric cooling system and pulse generator) are connected to a Raspberry Pi board that acts as controller.

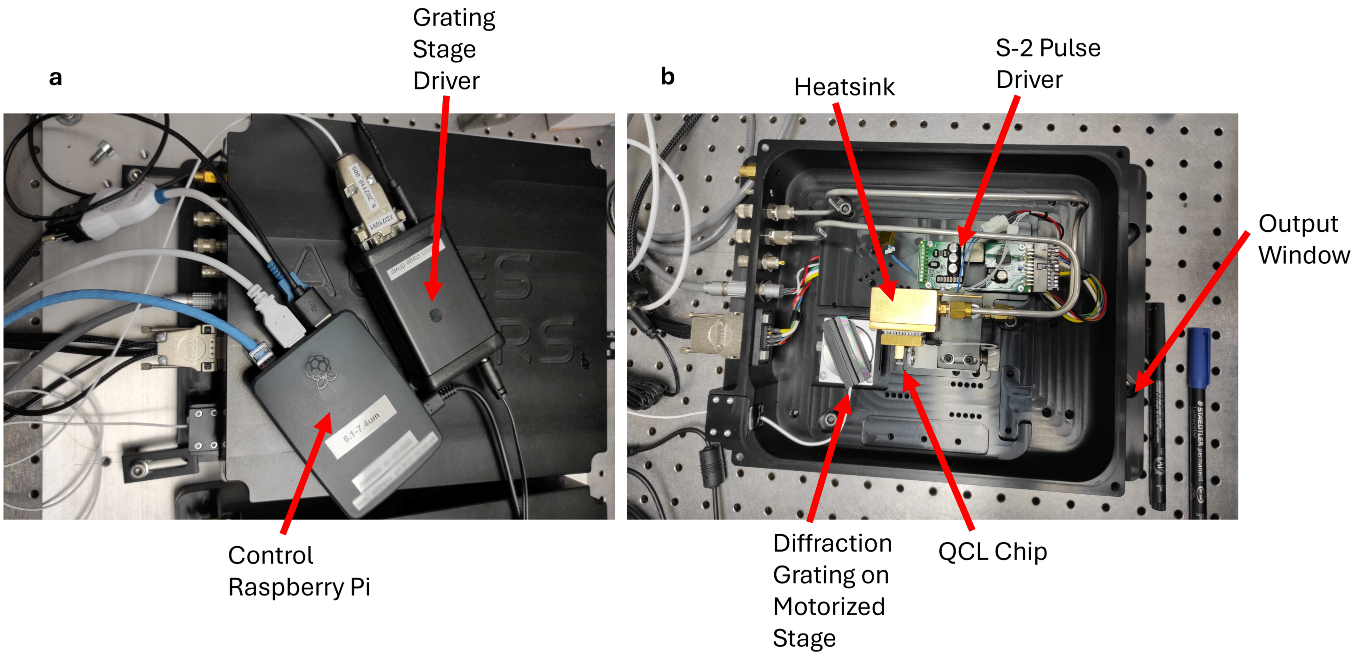

Figure 5.4: Photographs of the QCLs from Alpes Lasers and their **a** external and **b** internal components.

The duty cycle used for the excitation of the lasers has always been set to a maximum of 5% in order to protect the gain chip. Moreover, to avoid the overheating of the laser chip, a constant 18 °C temperature is ensured via a Peltier cooling system controlled by an Alpes Lasers TC-3 temperature controller.

5.2 Photodetector

Once the radiation source is determined, it is necessary to find a photodetector compatible with the emission range and characteristics of the QCLs. At such long wavelengths, there is a limited number of technologies available. After the commercially available photodetectors were compared, mercury cadmium telluride (MCT) technology was chosen because of its high and flat detectivity curves in the desired range and its assortment of commercially

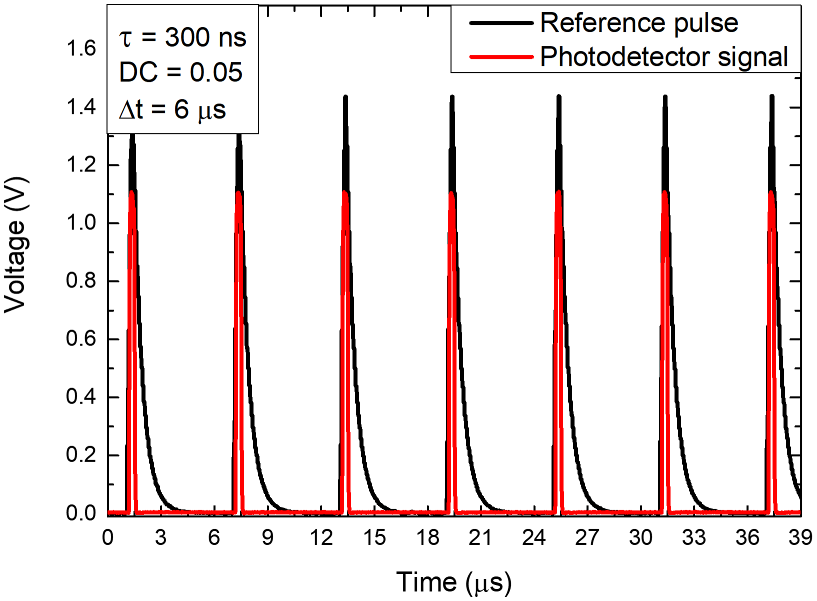

Figure 5.5: Laser pulses measured at the photodetector from the BG-6.1-7.4 QCL, working with a pulse width of 300 ns and a duty cycle of 0.05 (resulting in a 6 μs pulse separation), and the reference signal generated by the pulse generator of the QCL.

accessible detectors. Several technologies exist within MCT photodetectors, depending on the working principle of the device, the most common being photoconductive and photovoltaic detectors. In photoconductive detectors, the resistance of the active region is reduced under IR irradiation as a result of carrier excitation. These detectors are biased, so a change in the resistance will produce a change in the detected current. The working principle behind photovoltaic detectors is the detection of the photocurrent generated when light is absorbed in a semiconductor junction. Hence, they can work unbiased, eliminating the 1/f noise. Photoconductive detectors typically provide a linear response, in contrast to the complex current-voltage characteristics of photovoltaic detectors. Moreover, photoconductive detectors are more resistant to electrostatic discharge and cover a broader spectral range than their photovoltaic counterparts ("Vigo Photonics Catalog 2020/21", 2021). However, photovoltaic detectors operate faster and do not need an external bias.

Therefore, because of its linear response, high detectivity, and broad spectral range, the spectroscopy setup incorporates an MCT photoconductive detector (Vigo Photonics PCI-4TE-13) with a 4-stage Peltier cooling system, as well as a programmable preamplifier module (Vigo Photonics PIP-UC-LS).

Moreover, the photodetector counts with a GaAs hyperhemispheric immersion lens, which increases the optical area by 11 times while keeping the actual detector area small, as depicted in the schematics in Figure 5.6 . This results in an increase in the signal gathered by the detector, while keeping its physical area small, and thus maintaining low noise values. In

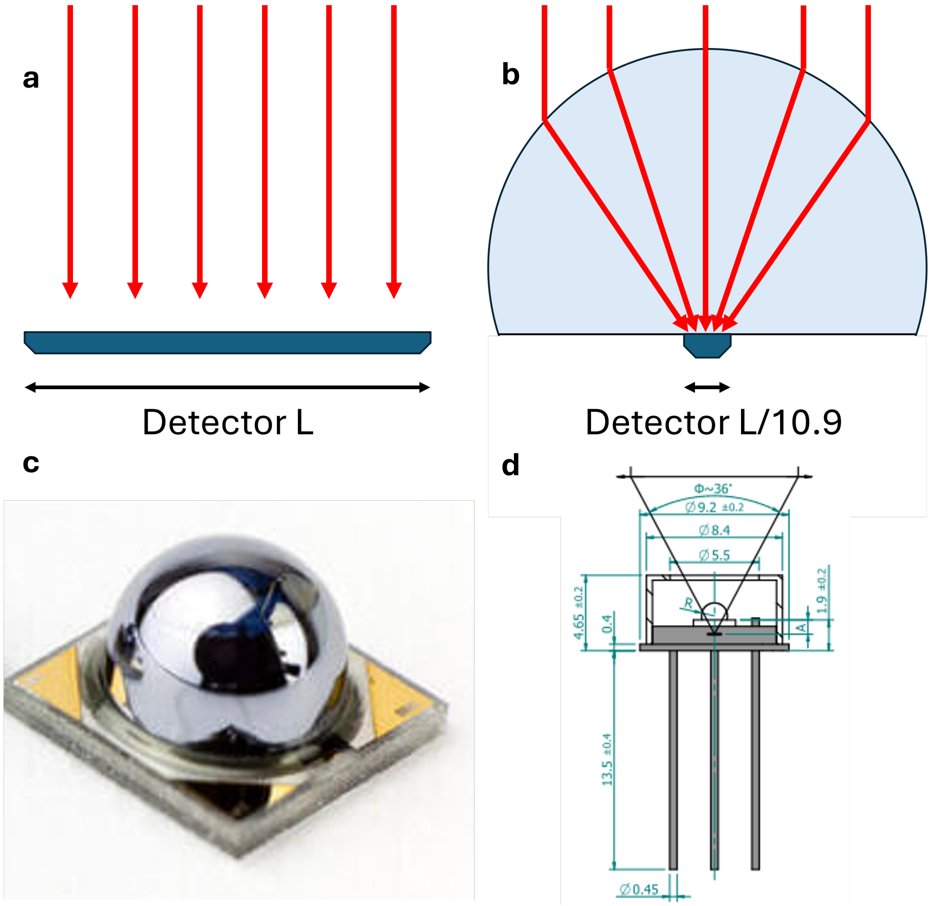

Figure 5.6: Schematics of light collection of a photodetector without (**a**) and with (**b**) a hyperhemispheric immersion lens. **c** Photograph of the hyperhemispheric GaAs immersion lens. **d** Technical drawing or the photodetector and the immersion lens. ((c) and (d) were extracted from "Vigo Photonics Catalog 2020/21", 2021; "Vigo Photonics: Immersion Lenses Technology", Last accessed 2024)

addition, the hyperhemispheric lens reduces the acceptance angle of the detector, filtering out background radiation, and therefore reducing the noise. The main drawback of the immersion lens is that it decreases the saturation power, but that does not pose a problem, since the signals measured at the detector are already attenuated by the optical elements and the reflection at the sample. The curves displayed in figure 5.7, show a current responsivity and a detectivityy above 0.5 A/W and $1.3 \cdot 10^9$ cm $\mathrm{Hz}^{1/2}$/W, respectively, in the whole spectral range of the QCLs.

The detector is integrated with an amplifier module (Vigo Photonics PIP-UC-LS), whose output is connected to an oscilloscope (Yokogawa DLM 2054), so the detected signal can be graphically visualised while adjusting the system, and to a lock-in amplifier (Zurich Instruments MFLI) with the reference signal from the pulser of the QCL as reference in order to acquire the data.

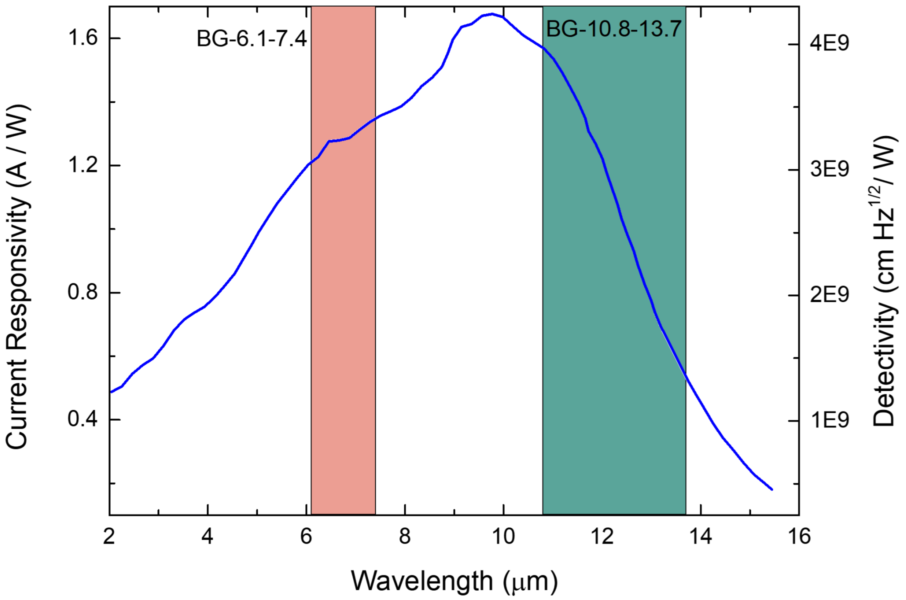

Figure 5.7: Current responsivity and detectivity curves of the PCI-4TE-13 MCT photodetector at 198 K, as provided by the manufacturer. The emission ranges of the QCLs in the setup are indicated in coloured regions.

5.3 Beam Path

Regarding the optics, several materials can be used to fabricate lenses for the mid-IR range thanks to their transparency in this range, like Ge or ZnSe, although the commercially available ZnSe lenses present slightly higher transparency than their Ge counterparts over a broader range. Alternatively, concave mirrors could also be used to focus light instead of lenses, reducing the incidence of chromatic aberration and providing a flat reflectance for all wavelengths, thus offering a stable spot size and position of the focal plane when acquiring spectra; but they would make the optical path more complex. A third option would be to use a Cassegrain objective, in which a convex mirror located in front of the aperture redirects incoming collimated light to a concave mirror set around it, which focusses light at a certain distance behind the convex mirror. This kind of system possesses the reduction of the chromatic aberration characteristic of reflective optics, along with a simplified design, since it can be acquired from an optics manufacturer as a single piece. However, the commercially available Cassegrain objectives offer smaller magnifications (up to 40x) than those achievable by refractive optics, and at a higher cost. Moreover, the convex mirror and its holder create an obscuration which reduces the light collected by the objective and alters the diffraction pattern of the spot. Because of all this, the light beam control has been made exclusively with refractive ZnSe optics.

The beam path has also been optimised with the aim of reducing the spot size at the sample for higher power density while also collecting as much radiation as possible at the photodetector.

For that, the optical setup depicted in Figure 5.8 has been implemented. The first task is to combine the beams coming from both QCLs and a visible (532 nm) alignment laser, so that the optical path is identical for all of them. This is achieved by using a beam combiner (4), transparent to QCL radiation but reflective to visible radiation, and two mirrors (5,6) to redirect the beam towards the path of the optical elements, the second of which (6) should be removed whenever QCL 1 (1) is used. In principle, light from the QCLs is linearly polarised in the direction perpendicular to the optical table. To ensure this polarisation, a ZnSe linear polariser (7) is introduced in the optical path. This polariser, which is placed on a rotary mount, also works as a variable light attenuator, since rotating its axis away from the polarisation axis of the QCLs will reduce their intensity following Malus's law $\mathrm{I} = \mathrm{I}_0 \cdot \cos\theta$.

According to the manufacturer, the QCL output beam has a spatial mode TEM_{00} ($\mathrm{M}^2 = 1.5$) with a beam diameter of 4 mm. The laser beam radius at the sample surface has been calculated for different commercially available ZnSe lenses using the following relation for the spot size of a focused beam (Bykov et al., 2013):

$$w_0 = \frac{4f\lambda M^2}{\pi D} + \frac{nD^3}{f^2}, \tag{5.1}$$

being f the focal length of the lens, D the incoming beam diameter and n the refractive index of the lens, and where the first term corresponds to the contribution from diffraction and the second to the contribution from spherical aberration.

Aspheric lenses, which drastically reduce the contribution from spherical aberration, have also been considered. Therefore, by neglecting the aberration term from Equation 5.1, it is clear that the larger the initial beam diameter, the smaller the beam diameter after the lens. Therefore, before focussing the beam, a keplerian beam expander is built (8,9). This beam expander consists of two plano-convex lenses, with their planar surfaces facing each other, and with a separation distance equal to the sum of their focal lengths. In this way, the first (objective) lens will focus the incoming collimated light into its focal plane, which will be gathered and collimated by the second (image) lens. The ratio between the original beam diameter and the resulting beam diameter, called the magnifying power (MP), will be equal to the ratio between the focal lengths of the lenses (Greivenkamp, 2004):

$$MP = \frac{f_i}{f_o} = \frac{D_i}{D_o}, \tag{5.2}$$

where $\mathrm{D_j}$ and $\mathrm{f_j}$ are the beam diameter and focal length, respectively, of the objective (o) and image (i) lenses, as illustrated in Figure 5.9.

Moreover, the most common diameter for mid-IR commercial refractive optics is 1 inch (25.4 mm). This imposes a restriction on the maximum beam diameter that can be generated with the beam expander without producing distortion due to diffraction. Therefore, since the beam as emitted by the QCLs has a diameter of 4 mm, the maximum acceptable MP value must be approximately 6. With this in mind, two plano-convex lenses of focal lengths of 25.4 mm (8) and 150 mm (9), separated by a distance of 175.4 mm, define a beam expander with MP = 5.9.

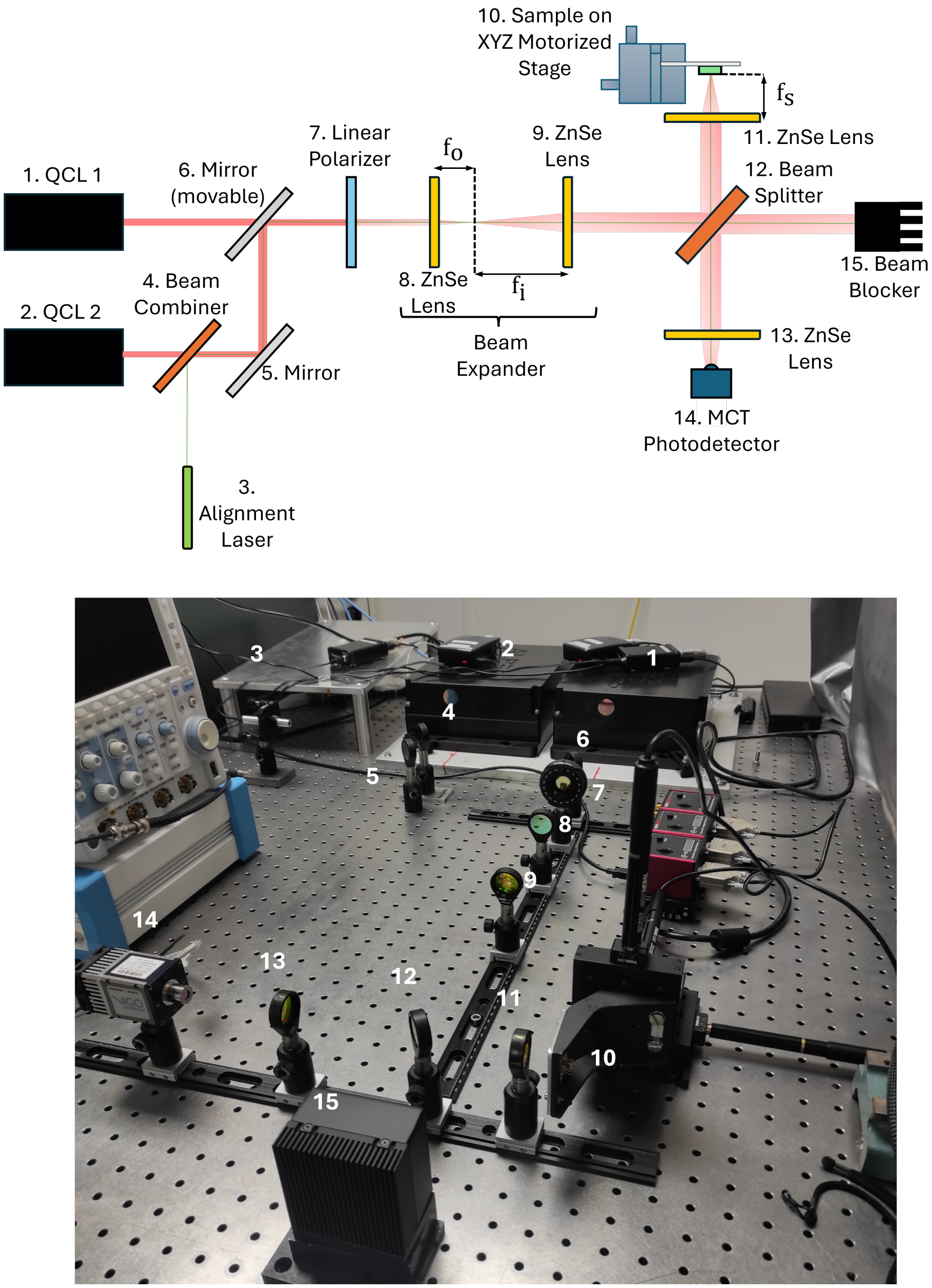

Figure 5.8: Optical path in the mid-IR spectroscopy and mapping setup.

Figure 5.10 shows the calculated beam diameter at the sample after focussing with different lenses in the whole wavelength range of the QCLs in this setup, with and without the use of the mentioned beam expander before the lens, that is, for 23.6 mm or 4 mm input beam diameter, respectively. In these graphs, three things are sought: first, a beam size as low as possible to increase the power density impinging on the sample; second, a lens that focusses the incoming radiation to a beam diameter as close as possible to 100 μm to focus on the

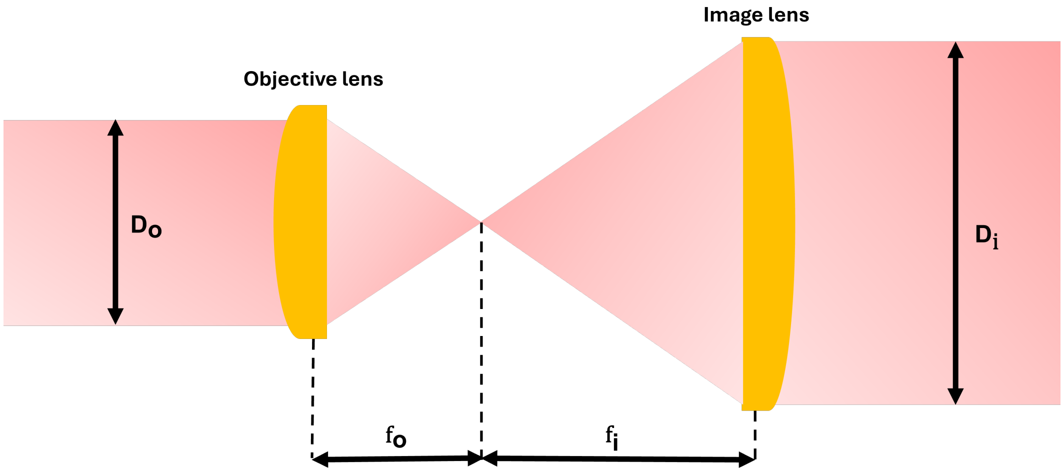

Figure 5.9: Working principle of a keplerian beam expander.

detector (which has this size) in order to collect as much light as possible in the detector; and third and last, that the size of the beam spot is as constant as possible for each of the lasers. Taking into account these considerations, an aspheric lens with a focal distance of 12.7 mm has been chosen to focus the beam on the sample (11), whereas before the detector (13), a plano-convex lens with a focal distance of 75 mm has been selected for QCL 1 (6.1-7.4 μm), and an aspheric lens of 50 mm focal distance for QCL 2 (10.8-13.7 μm). The two final elements of the optical setup are a 50:50 ZnSe beam splitter (12), suitable to work in the 7-14 μm range, and a beam blocker (15) to prevent the mid-IR radiation from leaving the limits of the optical table.

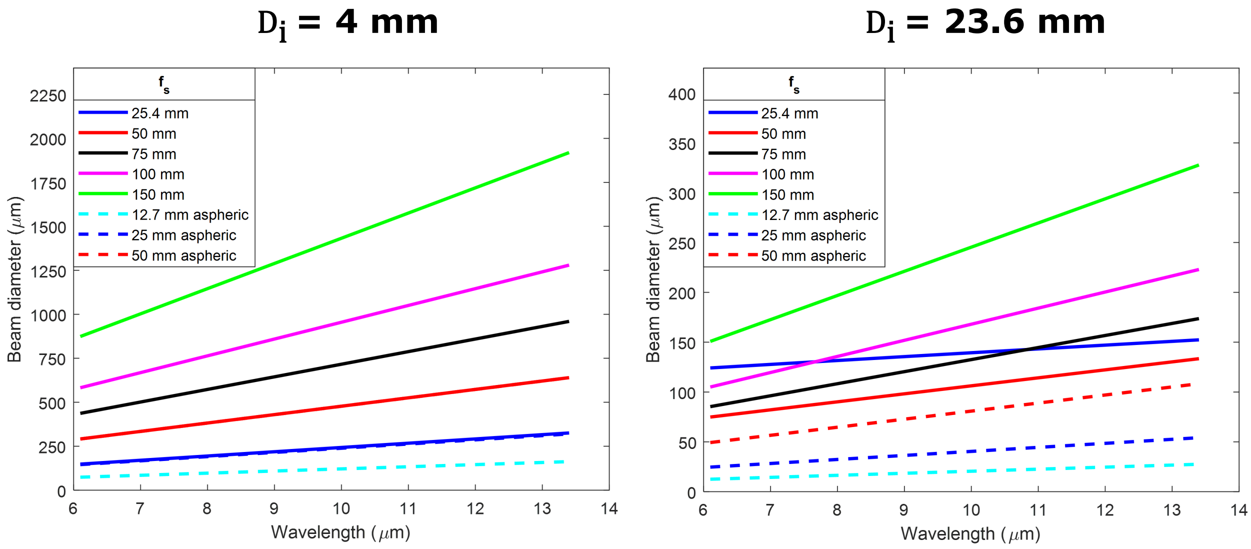
D_i = 4 mm

D_i = 23.6 mm

Figure 5.10: Beam diameter at the sample after focusing with lenses of different focal length f_s.

5.4 Computer Control

All electronic components of the setup (Raspberry Pi boards, lock-in amplifier, photodetector controller, and sample motorised stage controller) have been connected to a control computer to simplify their use and allow simultaneous operation of all of them through a script. Figure 5.11 shows a schematic of the connections between these components.

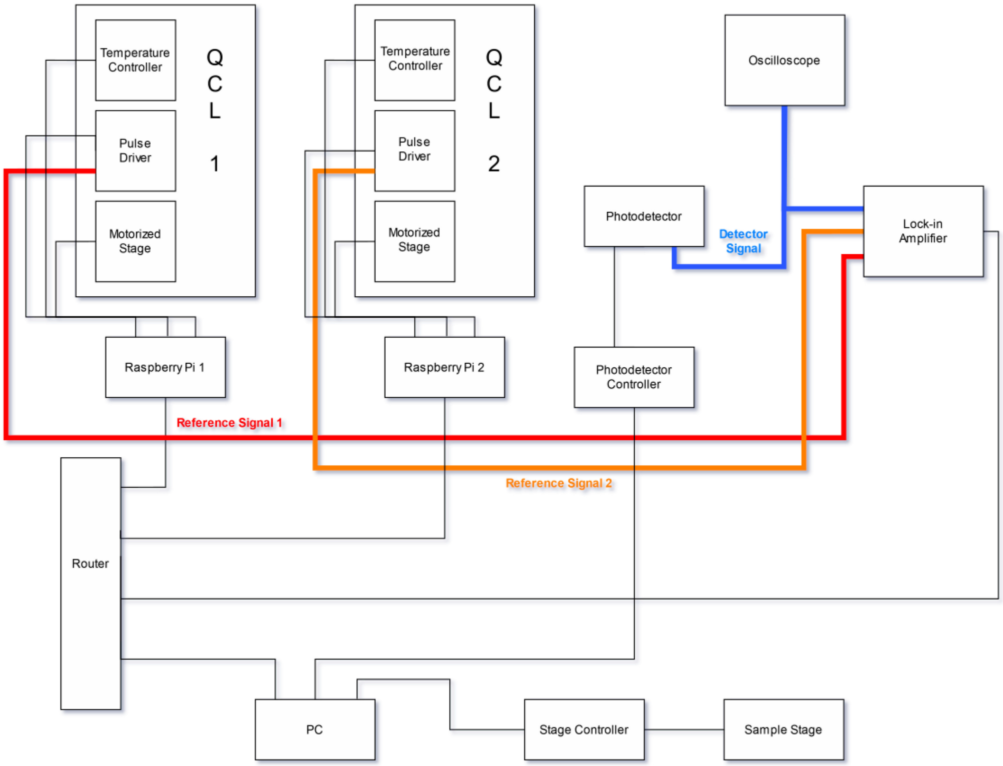

Figure 5.11: Schematic of the connections between the electronic components of the spectroscopy and mapping setup.

In order to perform spectral measurements, the response of the photodetector needs to be correlated to the wavelength at which the QCLs are emitting at each time. To accomplish this, a script has been developed that controls both the data acquisition from the lock-in amplifier and the elements of the QCL cavity. For that, it makes use of the zhinst library from Zurich Instruments ("Zurich Instruments Toolkit", Last accessed 2024), as well as the API from Alpes Lasers. It can set up the connection between the devices and the computer and apply the working conditions to the QCL (pulse duration, pulse frequency, applied voltage and heatsink temperature) and the lock-in amplifier (reference signal and demodulation scheme). Then, different functions have been created to perform sweeps with the QCL with either the wavenumber or the stage angle as a parameter, while storing the demodulator parameters from the lock-in at each step of the sweep and saving them to csv format.

5.5 Wavelength Calibration

Due to the continued usage of the QCLs, an offset between the desired angle of the diffraction grating and its actual value may appear, resulting in an artificial shift of the spectrum. This offset, as shown in Figure 5.12, can reach values as high as 100 cm^{-1}, leading to the loss of almost a third of the emission bandwidth, as well as great spectral inaccuracies, if not taken care of.

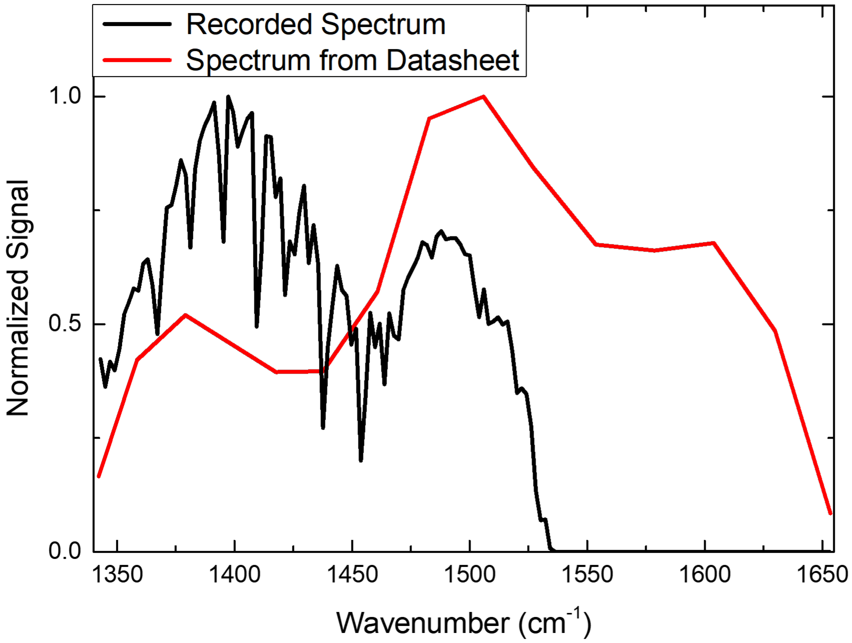

Figure 5.12: Measured emission spectrum of the BG-6.1-7.4 QCL compared to the one specified by the manufacturer, showing a clear wavenumber offset.

To correct for this offset, a new correspondence between the grating angle and the wavenumber needs to be found. For that, the absorption spectrum of a known sample, a polysterene calibration standard for infrared spectroscopy from the US National Institute of Standards and Technology (Gupta et al., 1995), was recorded with a FTIR spectrometer. The manufacturer's original angle-wavenumber calibration was then linearly interpolated to find the correspondent angle of the peaks measured in the FTIR. Finally, the spectrum of the same sample was measured as a function of the grating's diffraction angle, and the angular offset between the FTIR and the QCL spectra was calculated for each of the peaks analysed. The results, which are summarised in Table 5.1, show an angular offset of 2.26 ± 0.1 °. Therefore, the QCL angle calibration file was updated by downshifting the angles by the aforementioned offset, that is, for example, the angle at which a 1500 cm^{-1} wavenumber is achieved after the calibration is 105.1 °instead of the previous value of 107.4 °.

By applying this offset correction to the calibration file, both the polysterene absorption spectrum and the QCL emission spectrum are located in their expected values, as shown in

Peak	**FTIR** (cm^{-1})	**Interpolated angle** (°)	**QCL angle** (°)	**Difference** (°)
P_1	1372.73	104.24	101.91	2.33
P_2	1451.84	106.27	104.02	2.07
P_3	1492.47	107.20	104.93	2.27
P_4	1541.65	108.26	105.98	2.28
P_5	1584.41	109.11	106.79	2.32
P_6	1601.52	109.45	107.14	2.31

Table 5.1: Peaks of the calibration standard in the range of the BG-6.1-7.4 QCL.

Figure 5.13. Note that, especially in the emission spectrum of the QCL, although the position of the peak values is maintained, the relative heights between the bands are not. This is partially due to the lack of resolution in the spectrum provided by the QCL manufacturer. Another factor to take into account is the spectral dependence of the photodetector response and the transmittance of the optical components. Moreover, the bias applied to the QCL chip also plays a role: while the manufacturer records the spectrum at the optimum voltage value for each wavenumber, all the spectra presented in this chapter have been acquired at a constant voltage value of 16.6 V. Furthermore, since the spectra have been normalised to their respective maximum peak values so that they can be compared easily (the datasheet provides a measurement of the power emitted by the QCL, while the signal measured in this calibration process is the RMS value of the photodetector voltage after demodulation in the lock-in and with a different optical path), these differences have become more noticeable.

5.6 Mapping

The setup includes a xyz motorised stage to mount the sample, (10) in Figure 5.8. This stage allows to scan the sample with the QCLs. Figure 5.8 shows the reflection configuration that has been used, although a transmission geometry would also be possible. The motorised stage has a scanning resolution of 50 nm. However, the spatial resolution of the mapping will be limited by the spot size of the QCLs, as will be discussed along this section. Distinctive features such as a set of markers or the pads of the IDTs can be used to localise the spot on the sample, so that it can then be located at the points of interest within the sample. With the help of the motorised stage, a first adjustment is made to find the centre of the sample in terms of the coordinates of the motor, and fine focus alignment is performed by seeking the maximum reflected signal while moving the motor along the optical axis. Then, a first low-resolution reflection map can be acquired so that it covers a large area of the sample, such as the one displayed in Figure 5.14(a). This map was measured at the wavenumber of maximum emission from the QCL (1502 cm^{-1}) and with a motor step of 100 μm.

By comparing this map with the photograph in Figure 5.14 (b), different characteristics can be easily identified: three SAW devices at the centre of the image, a set of markers in a staircase form to the left of them (the bottom of which shows a metal square on top from the alignment between two lithographic processes), and even the washer used to hold the sample to the stage (top right corner). Therefore, this first map is more than sufficient to locate the devices in

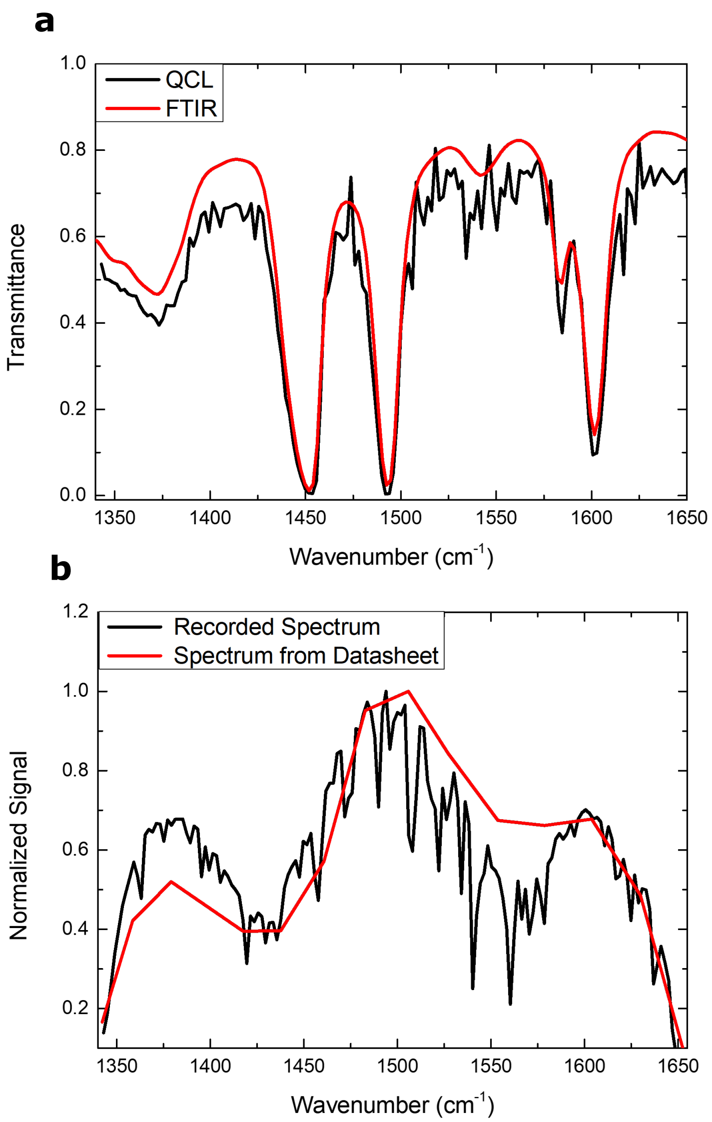

Figure 5.13: **a** Transmittance spectrum of the polysterene standard measured by FTIR spectroscopy and with the QCL after the offset correction. **b** Emission spectrum of the BG-6.1-7.4 QCL after the offset correction, both normalized to their maximum peak value for easier comparison.

the sample. See Figure 5.14(c) for the superimposed image of the map on top of the sample, showing great agreement with the shapes of the different features, as well as with the limits of the sample. In addition, reflection spectra were acquired at the Cr/Au contacts, as well as the bare $LiNbO_3$ sample, shown in Figure 5.14(d). These spectra, recorded at the blue and green dots in Figure 5.14(a) respectively, show that, as expected, the metal contacts reflect considerably more light than the $LiNbO_3$ substrate, helping for the search for a high-contrast wavelength for subsequent maps. For that, the ratio between these spectra was calculated and then multiplied by the emission spectrum of the QCL (contrast spectrum in Figure 5.14(d)), in such a way that the resulting spectrum contains information on the emission power (which

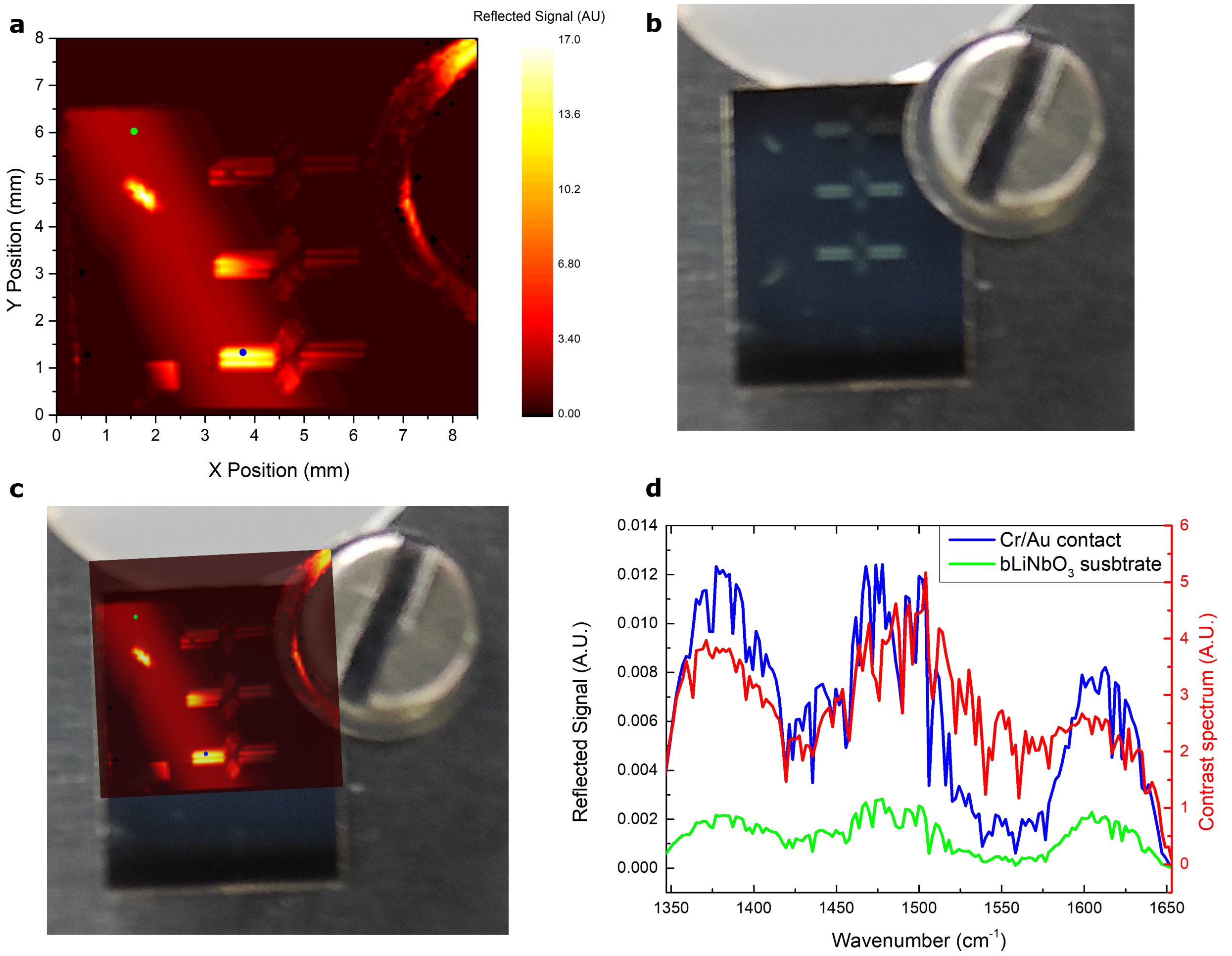

Figure 5.14: **a** Reflection map of a sample with SAW devices, acquired at a wavenumber of 1502 cm^{-1} and a motor step of 100 μm. **b** Photograph of the sample mapped with the QCL on the same mount used for the map. **c** Superposition of the reflection map and the photograph, showing great agreement. **d** Reflection spectra measured at spots marked by the blue and green dots in (a), as well as the contrast spectrum, defined as the reflection spectrum on gold divided by the reflection spectrum on LiNbO$_3$ and multiplied by the spectrum of the QCL .

contributes to the magnitude of the signal) and the reflection coefficients of both materials (which contribute to the contrast in the map). Then, the maximum of this spectrum was identified, being found at 1504 cm^{-1}.

In this way, a wavenumber of 1504 cm^{-1} (6.65 μm) has been selected for the following maps. The calculations in Figure 5.10 were used to determine that the approximate spot size for this wavelength, assuming perfect alignment, is 13.6 μm in diameter, so a slightly larger motor step size of 15 μm was chosen to map the sample. It has been noted that, the closer the chosen step size is to the diameter of the laser spot, the more accurate the sizes and distances will be in the map. On the other hand, the larger the step size, the faster the map can be generated. For reference, the map in Figure 5.14, which has a dimension of 80 steps x 85 steps, took approximately 4 hours to be recorded with an integration time of 0.6 seconds at each data point. With the original step size of 100 μm, this map was able to cover an area of 8 mm x 8.5 mm of the sample, although with a step size of 15 μm, providing the maximum spatial resolution, the area mapped in the same scanning time would be of only 1.2 mm x 1.275 mm. However, the first map provides enough resolution to identify the devices all accross the sample in a single scan.

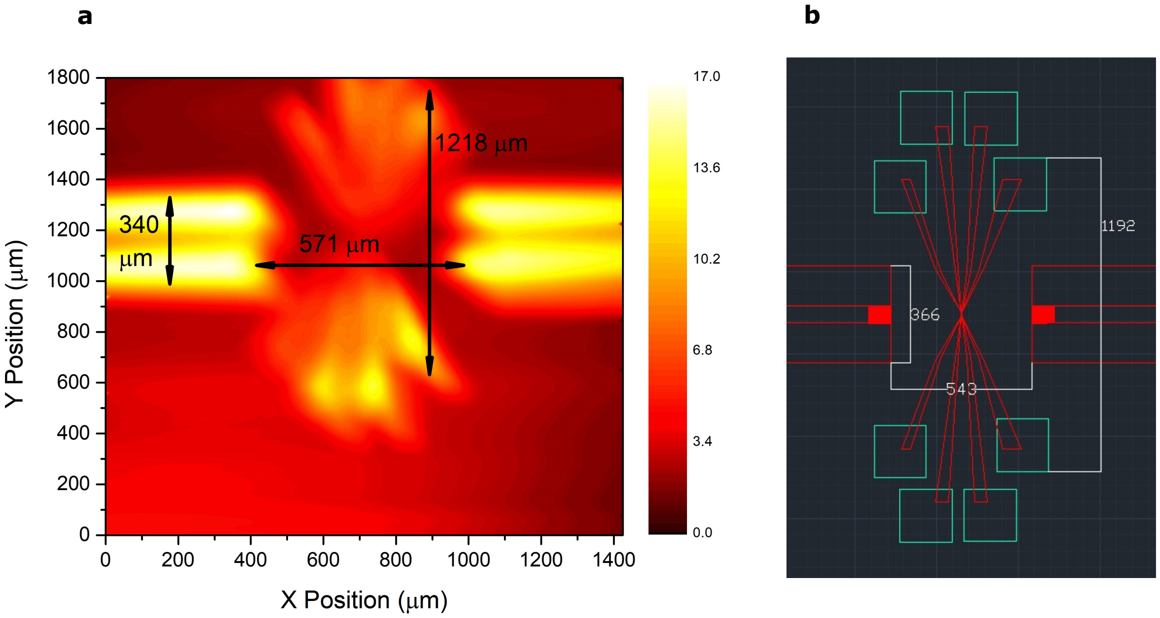

Figure 5.15: **a** Reflection map of a SAW device, acquired at a wavenumber of 1504 cm^{-1} and a motor step of 15 μm. Approximated measurements of some distances are displayed on top. **b** CAD design of the device mapped in (a) with annotations to compare to the distances measured.

Therefore, an initial protocol can be established as follows: a first map of a large area of the sample with low resolution is used to identify the regions where to perform later on higher resolution maps of a smaller portion of the sample. Figure 5.15 presents a map of the area around one of the SAW devices (a), as well as the CAD design of the device (b). Although the image lacks sharpness and some elements, such as the fine part of the metal contacts or the fingers of the IDTs, cannot be resolved because of their reduced size, it is enough to define the regions inside and outside of the SAW beam path. Moreover, the distances measured in the reflection map match already the measurements from the CAD file with a maximum deviation of 7% in the smallest distance checked, so the chosen step size, although not exactly the same, is close to the actual beam diameter.

Chapter 6

Conclusions and Future Work

6.1 Conclusions

In Chapter 3, the fabrication of two-port SAW resonators in the GHz frequency range on $LiNbO_3$ substrates has been addressed, optimising their design parameters for their use in combination with graphene Hall bars for acoustoelectric transport experiments. In addition to the observation of the well-known acoustoelectric voltage created along the SAW propagation direction, an additional voltage has been detected in the transverse direction. This voltage was expected to arise due to the strain-induced pseudo-magnetic (or gauge) field generated by the SAW in the graphene sheet, in a similar way as reported in graphene under static strain. However, the observation of this pseudo-Hall voltage in SAW devices in graphene has been reported during the realisation of this thesis by another research group (P. Zhao et al., 2022) using devices similar to the ones presented here. Both acoustoelectric and pseudo-Hall voltages have been also confirmed to present a linear dependence with the acoustic power in the fabricated devices. Moreover, with the aim of studying the role of the carrier density and type in these acoustoelectric effects in graphene, $LiNbO_3$ thin-film-based heterostructures with a buried gate have been explored. A 5-µm-thick $LiNbO_3$ layer, bonded to a bulk $LiNbO_3$ substrate through a Cr/Au/Cr interlayer, has been proven to be well-suited for acoustoelectric devices, although with just a moderate modulation of the conductivity of graphene, not enough to reach the objective of accessing the CNP.

In Chapter 4, a novel plasmonic biosensor has been theoretically demonstrated, where the local dynamic modulation of the active surface induced by an on-chip electrically-controlled two-port SAW resonator acts as a virtual diffraction grating allowing to couple far-field light into propagating surface polaritons without any patterning. A TMM-tailored gated graphene-based van der Waals heterostructure permits to generate and tune surface plasmon-phonon polaritons across the mid-infrared range covering the vibrational resonances of most organic compounds. The device has been theoretically investigated for fingerprinting ultrathin biolayers via SEIRA spectroscopy, proving its sensitivity down to the ML limit. The plasmonic response of the acoustically-rippled surface has been tested with various analytes, including thin films (down to a ML) of CBP, an organic semiconductor with sharp and intense absorption lines, as well as biological compounds with broad and weak absorption bands such as A/G-IgG protein bilayers and VGA peptide MLs. The COM analysis demonstrates that the biosensor response is able to elucidate the presence of extremely thin analyte layers in all cases, even when a faint interaction between the vibrational resonances of the molecules and the polaritons does not lead to a Fano resonance but only to a resonance broadening. All these results are reported in Izquierdo-López et al., 2023.

In Chapter 5, a home-built laser-based mid-IR spectroscopy and mapping setup has been designed and implemented using off-the-shelf components. Two external-cavity QCLs operating in the 6-14 μm range have been combined with a photoconductive MCT detector. The refractive ZnSe optical elements in the beam path have been selected to minimise the spot size at the sample, while optimising light collection at the photodetector. In addition, a motorised xyz stage allows the sample to be scanned for mapping the areas of interest. A Python script has been written to control and coordinate the action of the different components of the setup. The pulses driving the QCL emission are used for the photodetection using a lock-in amplifier. The setup has been spectrally calibrated and tested in the acquisition of reflectance and transmittance spectra, as well as in mapping the sample for the location of the plasmonic devices. The setup developed is capable of focusing mid-IR laser beams of 4 mm in diameter down to a minimum spot size of 15 μm on the sample surface, which determines the mapping resolution. The high power density of the laser spot together with the scanning capability of the setup paves the way for the study of advanced plasmonic devices in graphene, such as the SAW-assisted biosensors devised in Chapter 4.

In summary, three different effects of SAWs on graphene have been studied in this thesis. First, the interaction of the charge carriers in graphene with the piezoelectric field of the SAW, leading to the acoustoelectric transport of carriers in the direction of SAW propagation. Second, the distortion of the electronic dispersion of graphene by the strain field of the SAW, causing the emergence of a pseudo-Hall voltage in the direction transverse to the SAW propagation as a consequence of the strain-induced pseudo-magnetic or gauge field arising in graphene. Third, the effect of SAWs on graphene solely as a result of the surface deformation. In this case, SAWs can act as a virtual diffraction grating that couples far-field light into SPP(P)s. A SAW-assisted mid-IR graphene plasmonic biosensor relying on this phenomenon has been theoretically demonstrated for fingerprinting ultrathin biolayers, and a mid-IR spectroscopy setup has been assembled and tested with the objective of experimentally developing plasmonic devices based on van der Waals heterostructures such as the designed biosensor. Moreover, this thesis has resulted in several articles and conference contributions, which are listed in Appendix B.

6.2 Future Work

The heterostructure based on thin-film $LiNbO_3$ studied in Chapter 3 opens the possibility for deeper studies on the nature of the interaction between SAWs and graphene or other 2D materials. However, further investigation needs to be performed on this kind of structures in order to enhance the modulation of the Fermi level of graphene so that full electrical control is achieved through the field-effect. Moreover, the dependence of the acoustoelectric and pseudo-Hall transport on the SAW wavelength can be analysed by either fabricating devices with different SAW wavelength or by optimising chirped IDTs to provide flat transmission bands over an extended wavelength range. On the other hand, the analysis of the effect of charge carriers on the SAWs, that is the attenuation/gain produced in the SAW propagation, paves the way for developing active graphene/$LiNbO_3$ SAW devices for signal processing and communication applications.

Furthermore, novel strategies are foreseen to quantify the magnitude of the SAW-induced pseudo-magnetic field in future experiments. So far, the strategy reported by P. Zhao et al., 2022 was based on an external magnetic field causing a Hall voltage opposing the SAW-induced pseudo-Hall voltage, varying the magnitude of this external field until the pseudo-Hall voltage was neutralised. A simpler strategy not requiring a magnetic field would take advantage of a standing wave in the two-port SAW resonator (so that no net acoustoelectric current is generated). In this case, an external current would be applied between two contacts in the longitudinal direction, so that the pseudo-magnetic field can be estimated from the pseudo-Hall voltage measured in the transverse direction, as in a regular Hall transport measurement. Another strategy, permitting to reduce the number of probes needed, would be to perform measurements using alternative geometries such as Corbino discs.

Regarding the biosensor described in Chapter 4, the study presented here paves the way for the development of advanced SAW-assisted LOC systems combining the chemical fingerprinting capability of this novel sensor with complementary SAW-mediated physical sensing mechanisms (Ballantine, 1997) and SAW-driven microfluidic capabilities (droplet streaming, mixing, etc.) (Wixforth, 2003; Ding et al., 2013) previously reported in the literature. In a different approach, the proposed biosensor could be adapted to work in a liquid environment by using an AlN crystal orientation providing a shear-horizontal SAW (Love mode) instead of a sagittal SAW (Rayleigh mode) (G. Hu et al., 2007) or even by combining both at different in-plane propagation directions (Kobayashi et al., 1995).

Moreover, the sensitivity of the experimental implementation of the biosensor might be enhanced by enabling an alternated in-phase and out-of-phase modulation of the optical excitation and the RF signal fed to the IDT for creating the SAW. This method, which strongly suppresses the influence of thermal or laser power fluctuations, allows to increase the signal to noise ratio (Fandan et al., 2020).

Furthermore, a software can be created to fit experimental SEIRA via the COM. This software would be complemented by a library of analytes built by extracting the frequency and linewidth of their vibrational resonances from spectroscopic measurements.

Finally, with respect to the mid-IR setup for spectroscopy and imaging described in Chapter 5, several improvements are already planned, such as the enclosure of the system in a chamber with a N_2 inlet for purging the air in order to reduce the influence of water vapour on the acquired spectra. In addition, the initial inspection of the sample will be eased by the addition of a visible light source combined with an objective and a CCD camera. The developed setup will be soon used for the development and study of plasmonic devices in the mid-IR range, such as the SAW-assisted graphene plasmonic biosensor described in Chapter 4.

References

Adato, R., & Altug, H. (2013). *Nature Communications*, *4*(1), 2154.

Alpes Lasers. (Last accessed 2024). https://www.alpeslasers.ch/products/#lasers

Arsenovic, A., Hillairet, J., Anderson, J., Forsten, H., Ries, V., Eller, M., Sauber, N., Weikle, R., Barnhart, W., & Forstmayr, F. (2022, January). Scikit-rf: An open source python package for microwave network creation, analysis, and calibration. https://doi.org/10.1109/MMM.2021.3117139

Autore, M., Li, P., Dolado, I., Alfaro-Mozaz, F. J., Esteban, R., Atxabal, A., Casanova, F., Hueso, L. E., Alonso-González, P., Aizpurua, J., Nikitin, A. Y., Vélez, S., & Hillenbrand, R. (2018). Boron nitride nanoresonators for phonon-enhanced molecular vibrational spectroscopy at the strong coupling limit. *Light, Science & Applications*, *7*(4), 17172. https://doi.org/10.1038/lsa.2017.172

Baker, M. J., Trevisan, J., Bassan, P., Bhargava, R., Butler, H. J., Dorling, K. M., Fielden, P. R., Fogarty, S. W., Fullwood, N. J., Heys, K. A., Hughes, C., Lasch, P., Martin-Hirsch, P. L., Obinaju, B., Sockalingum, G. D., Sulé-Suso, J., Strong, R. J., Walsh, M. J., Wood, B. R., … Martin, F. L. (2014). Using Fourier transform IR spectroscopy to analyze biological materials. *Nature Protocols*, *9*(8), 1771–1791. https://doi.org/10.1038/nprot.2014.110

Ballantine, D. S. (1997). *Acoustic Wave Sensors*. Academic Press.

Bandhu, L., Lawton, L. M., & Nash, G. R. (2013). Macroscopic acoustoelectric charge transport in graphene. *Applied Physics Letters*, *103*(13). https://doi.org/10.1063/1.4822121

Bandhu, L., & Nash, G. R. (2014). Temperature dependence of the acoustoelectric current in graphene. *Applied Physics Letters*, *105*(26). https://doi.org/10.1063/1.4905222

Bandhu, L., & Nash, G. R. (2016). Controlling the properties of surface acoustic waves using graphene. *Nano Research*, *9*(3), 685–691. https://doi.org/10.1007/s12274-015-0947-z

Barker, A. S., & Loudon, R. (1967). Dielectric Properties and Optical Phonons in LiNbO3. *Physical Review*, *158*, 433–445. https://doi.org/10.1103/PhysRev.158.433

Barth, A. (2007). Infrared spectroscopy of proteins. *Biochimica et Biophysica Acta*, *1767*(9), 1073–1101. https://doi.org/10.1016/j.bbabio.2007.06.004

Beck, S., Gerbert, D., Glaser, T., & Pucci, A. (2015). Charge transfer at organic/inorganic interfaces and the formation of space charge regions studied with infrared light. *Journal of Physical Chemistry C*, *119*(22), 12545–12550. https://doi.org/10.1021/acs.jpcc.5b04398

Bleu, Y., Bourquard, F., Loir, A.-S., Barnier, V., Garrelie, F., & Donnet, C. (2019). Raman study of the substrate influence on graphene synthesis using a solid carbon source via rapid thermal annealing. *Journal of Raman spectroscopy*, *50*(11), 1630–1641. https://doi.org/10.1002/jrs.5683

Block Engineering. (Last accessed 2024). https://www.blockeng.com/applications/lasers.html

Boscá, A., Pedrós, J., Martínez, J., Calle, F., & Palacios, T. (2015, November). Procedimiento de transferencia de nanocapas y aparato de realización del mismo (Method for transferring nanolayers and apparatus for carrying our said method). https://doi.org/PCT/ES2014/070859

Boscá, A., Ladrón-de-Guevara, A., Pedros, J., Martínez, J., Fandan, R., & Calle, F. (2023). Parameter space for chemical vapor deposition graphene in cold-wall reactors under high precursor flow rate. *Crystal Growth & Design*, *23*(9), 6349–6358. https://doi.org/10.1021/acs.cgd.3c00258

Boscá, A., Pedrós, J., Martínez, J., & Calle, F. (2015). Method for extracting relevant electrical parameters from graphene field-effect transistors using a physical model. *Journal of Applied Physics*, *117*(4). https://doi.org/10.1063/1.4906972

Boscá, A., Pedrós, J., Martínez, J., Palacios, T., & Calle, F. (2016). Automatic graphene transfer system for improved material quality and efficiency. *Scientific reports*, *6*(1), 21676. https://doi.org/10.1038/srep21676

Brar, V. W., Jang, M. S., Sherrott, M., Lopez, J. J., & Atwater, H. A. (2013). Highly confined tunable mid-infrared plasmonics in graphene nanoresonators. *Nano Letters*, *13*(6), 2541–2547. https://doi.org/10.1021/nl400601c

Bruker Guide to FTIR Microsocopy. (Last accessed 2024). https://www.bruker.com/en/products-and-solutions/infrared-and-raman/ft-ir-microscopes/what-is-ft-ir-microscopy.html

Bykov, S. V., Sharma, B., & Asher, S. A. (2013). High-Throughput, High-Resolution Echelle Deep-UV Raman Spectrometer. *Applied Spectroscopy*, *67*(8), 873–883. https://doi.org/10.1366/12-06960

Caldwell, J. D., Lindsay, L., Giannini, V., Vurgaftman, I., Reinecke, T. L., Maier, S. A., & Glembocki, O. J. (2015). Low-loss, infrared and terahertz nanophotonics using surface phonon polaritons. *Nanophotonics*, *4*(1), 44–68. https://doi.org/10.1515/nanoph-2014-0003

Campbell, C. (1989). *Surface acoustic wave devices and their signal processing applications*. Academic Press.

Campbell, C. K. (1998). *Surface Acoustic Wave Devices for Mobile and Wireless Communications* (1st ed.). Academic Press.

Carmichael, C. P., Smith, M. S., Weeks, A. R., & Malocha, D. C. (2018). Experimental investigation of surface acoustic wave acoustoelectric effect using a graphene film on lithium niobate. *IEEE Transactions on Ultrasonics, Ferroelectrics, and Frequency Control*, *65*(11), 2205–2207. https://doi.org/10.1109/TUFFC.2018.2870042

Cattoni, A., Mailly, D., Dalstein, O., Faustini, M., Seniutinas, G., Rösner, B., & David, C. (2018). Sub-10 nm electron and helium ion beam lithography using a recently developed alumina resist. *Microelectronic Engineering*, *193*, 18–22. https://doi.org/10.1016/j.mee.2018.02.015

Chen, Y., Shu, Z., Zhang, S., Zeng, P., Liang, H., Zheng, M., & Duan, H. (2021). Sub-10 nm fabrication: Methods and applications. *International Journal of Extreme Manufacturing*, *3*(3), 32002. https://doi.org/10.1088/2631-7990/ac087c

Clementi, G., Ouhabaz, M., Margueron, S., Suarez, M. A., Bassignot, F., Gauthier-Manuel, L., Belharet, D., Dulmet, B., & Bartasyte, A. (2021). Highly coupled and low frequency vibrational energy harvester using lithium niobate on silicon. *Applied Physics Letters*, *119*(1). https://doi.org/10.1063/5.0052615

Collins, J. H., Lakin, K. M., Quate, C. F., & Shaw, H. J. (1968). Amplification of acoustic surface waves with adjacent semiconductor and piezoelectric crystals. *Applied Physics Letters*, *13*(9), 314–316. https://doi.org/10.1063/1.1652628

Costanza, M., Spina, L. L., Moreira, A. D. S. L., Belharet, D., Bartasyte, A., & Margueron, S. (2023). Acousto-electric measurements at 2.5 GHz on graphene transferred onto YX128°-LiNbO3. *Nanotechnology*, *34*(32). https://doi.org/10.1088/1361-6528/acd063

Dai, S., Fei, Z., Ma, Q., Rodin, A. S., Wagner, M., McLeod, A. S., Liu, M. K., Gannett, W., Regan, W., Watanabe, K., Taniguchi, T., Thiemens, M., Dominguez, G., Neto, A. H. C., Zettl, A., Keilmann, F., Jarillo-Herrero, P., Fogler, M. M., & Basov, D. N. (2014). Tunable phonon polaritons in atomically thin van der waals crystals of boron nitride. *Science*, *343*(6175), 1125–1129. https://doi.org/10.1126/science.1246833

Daylight Solutions. (Last accessed 2024). https://www.daylightsolutions.com/products

Dazzi, A., & Prater, C. B. (2017). AFM-IR: Technology and applications in nanoscale infrared spectroscopy and chemical imaging. *Chemical Reviews*, *117*(7), 5146–5173. https://doi.org/10.1021/acs.chemrev.6b00448

Ding, X., Li, P., Lin, S.-C. S., Stratton, Z. S., Nama, N., Guo, F., Slotcavage, D., Mao, X., Shi, J., Costanzo, F., & Huang, T. J. (2013). Surface acoustic wave microfluidics. *Lab on a chip*, *13*(18), 3626–3649. https://doi.org/10.1039/c3lc50361e

Duarte, F. J. (1995). *Tunable lasers handbook* (1st ed.). Academic Press.

Dubos, R. J., & Hotchkiss, R. D. (1941). The production of bactericidal substances by aerobic sportulatig bacilli. *Journal of Experimental Medicine*, *73*(5), 629–640. https://doi.org/10.1084/jem.73.5.629

Eliasson, M., Olsson, A., Palmcrantz, E., Wiberg, K., Inganäs, M., Guss, B., Lindberg, M., & Uhlén, M. (1988). Chimeric igg-binding receptors engineered from staphylococcal protein a and streptococcal protein g. *Journal of Biological Chemistry*, *263*(9), 4323–4327. https://doi.org/10.1016/S0021-9258(18)68928-8

Epps, H. L. V. (2006). René dubos: Unearthing antibiotics. *The Journal of Experimental Medicine*, *203*(2), 259. https://doi.org/10.1084/jem.2032fta

Fandan, R., Pedrós, J., Schiefele, J., Boscá, A., Martínez, J., & Calle, F. (2018). Acoustically-driven surface and hyperbolic plasmon-phonon polaritons in graphene/h-bn heterostructures on piezoelectric substrates. *Journal of Physics D: Applied Physics*, *51*(20), 204004. https://doi.org/10.1088/1361-6463/aab8bd

Fandan, R. (2020). *Quasiparticles in graphene and other 2D materials: modulation by a Surface acoustic wave and contribution to Coulomb drag, a PhD thesis*, ETSIT-UPM. https://doi.org/10.20868/UPM.thesis.65493

Fandan, R., Pedrós, J., & Calle, F. (2021). Exciton–Plasmon Coupling in 2D Semiconductors Accessed by Surface Acoustic Waves. *ACS Photonics*, *8*(6), 1698–1704. https://doi.org/10.1021/acsphotonics.1c00173

Fandan, R., Pedrós, J., Hernández-Mínguez, A., Iikawa, F., Santos, P. V., Boscá, A., & Calle, F. (2020). Dynamic local strain in graphene generated by surface acoustic waves. *Nano Letters*, *20*(1), 402–409. https://doi.org/10.1021/acs.nanolett.9b04085

Fang, T., Konar, A., Xing, H., & Jena, D. (2007). Carrier statistics and quantum capacitance of graphene sheets and ribbons. *Applied Physics Letters*, *91*(9), 092109–3. https://doi.org/10.1063/1.2776887

Fang, Z., Wang, Y., Schlather, A. E., Liu, Z., Ajayan, P. M., de Abajo, F. J. G., Nordlander, P., Zhu, X., & Halas, N. J. (2014). Active tunable absorption enhancement with graphene nanodisk arrays. *Nano Letters*, *14*(1), 299–304. https://doi.org/10.1021/nl404042h

Fazio, D. D., Purdie, D. G., Ott, A. K., Braeuninger-Weimer, P., Khodkov, T., Goossens, S., Taniguchi, T., Watanabe, K., Livreri, P., Koppens, F. H. L., Hofmann, S., Goykhman, I., Ferrari, A. C., & Lombardo, A. (2019). High-mobility, wet-transferred graphene grown by chemical vapor deposition. *ACS Nano*, *13*(8), 8926–8935. https://doi.org/10.1021/acsnano.9b02621

Fei, Z., Andreev, G. O., Bao, W., Zhang, L. M., McLeod, A. S., Wang, C., Stewart, M. K., Zhao, Z., Dominguez, G., Thiemens, M., Fogler, M. M., Tauber, M. J., Castro-Neto, A. H., Lau, C. N., Keilmann, F., & Basov, D. N. (2011). *Nano Letters*, *11*(11), 4701–4705.

Ferrari, A. C., Meyer, J. C., Scardaci, V., Casiraghi, C., Lazzeri, M., Mauri, F., Piscanec, S., Jiang, D., Novoselov, K. S., Roth, S., & Geim, A. K. (2006). Raman spectrum of graphene and graphene layers. *Physical Review Letters*, *97*(18), 187401. https://doi.org/10.1103/physrevlett.97.187401

Fingerprinting biomolecules with the help of sound. (Last accessed 2024). https://phys.org/news/2024-01-fingerprinting-biomolecules.html

Foti, S. (2015). *Surface wave methods for near-surface site characterization* (1st ed.). CRC Press. https://doi.org/10.1201/b17268

GenISys GmbH. (Last accessed 2024). https://www.genisys-gmbh.com/

Graphenea. (Last accessed 2024). *Monolayer Graphene on Cu – Graphenea*. https://www.graphenea.com/collections/buy-graphene-films/products/monolayer-graphene-on-cu-4-inches

Greivenkamp, J. E. (2004). *Field guide to geometrical optics* (Vol. 1). SPIE Optical Engineering Press.

Guinea, F., Katsnelson, M. I., & Vozmediano, M. A. H. (2008). Midgap states and charge inhomogeneities in corrugated graphene. *Physical Review B: Condensed Matter and Materials Physics*, *77*(7). https://doi.org/10.1103/PhysRevB.77.075422

Gupta, D., Wang, L., Hanssen, L., Hsia, J., & Datla, R. (1995). Standard reference materials: Polystyrene films for calibrating the wavelength scale of infrared spectrophotometers.

Hackett, L., Miller, M., Weatherred, S., Arterburn, S., Storey, M. J., Peake, G., Dominguez, D., Finnegan, P. S., Friedmann, T. A., & Eichenfield, M. (2023). Non-reciprocal acoustoelectric microwave amplifiers with net gain and low noise in continuous operation. *Nature Electronics*. https://doi.org/10.1038/s41928-022-00908-6

Harata, A., Nishimura, H., & Sawada, T. (1990). Laser-induced surface acoustic waves and photothermal surface gratings generated by crossing two pulsed laser beams. *Applied Physics Letters*, *57*(2), 132–134. https://doi.org/10.1063/1.103964

Hayden, J., Hugger, S., Fuchs, F., & Lendl, B. (2018). A quantum cascade laser-based Mach–Zehnder interferometer for chemical sensing employing molecular absorption and dispersion. *Applied physics. B, Lasers and Optics*, *124*(2), 1–9. https://doi.org/10.1007/s00340-018-6899-8

Hermann, D. R., Ramer, G., Kitzler-Zeiler, M., & Lendl, B. (2022). Quantum cascade laser-based vibrational circular dichroism augmented by a balanced detection scheme. *Analytical chemistry*, *94*(29), 10384–10390. https://doi.org/10.1021/acs.analchem.2c01269

Hernández-Mínguez, A., Liou, Y.-T., & Santos, P. V. (2018). Interaction of surface acoustic waves with electronic excitations in graphene. *Journal of Physics D: Applied Physics*, *51*(38), 383001. https://doi.org/10.1088/1361-6463/aad593

Hernández-Mínguez, A., Tahraoui, A., Lopes, J. M. J., & Santos, P. V. (2016). Acoustoelectric transport at gigahertz frequencies in coated epitaxial graphene. *Applied Physics Letters*, *108*(19). https://doi.org/10.1063/1.4949756

Hu, G., Xu, J., Auner, G. W., Smolinski, J., & Ying, H. (2007). *Electronics Letters*, *43*(18), 1006–1007.

Hu, H., Yang, X., Zhai, F., Hu, D., Liu, R., Liu, K., Sun, Z., & Dai, Q. (2016). Far-field nanoscale infrared spectroscopy of vibrational fingerprints of molecules with graphene plasmons. *Nature Communications*, *7*(1), 12334. https://doi.org/10.1038/ncomms12334

Huck, C., Neubrech, F., Vogt, J., Toma, A., Gerbert, D., Katzmann, J., Härtling, T., & Pucci, A. (2014). Surface-enhanced infrared spectroscopy using nanometer-sized gaps. *ACS Nano*, *8*(5), 4908–4914. https://doi.org/10.1021/nn500903v

Hutson, A. R., McFee, J. H., & White, D. L. (1961). Ultrasonic Amplification in CdS. *Physical Review Letters*, *7*(6), 237–239. https://doi.org/10.1103/PhysRevLett.7.237

Ingebrigtsen, K. A. (1970). Linear and nonlinear attenuation of acoustic surface waves in a piezoelectric coated with a semiconducting film. *Journal of Applied Physics*, *41*(2), 454–459. https://doi.org/10.1063/1.1658696

Insepov, Z., Emelin, E., Kononenko, O., Roshchupkin, D. V., Tnyshtykbayev, K. B., & Baigarin, K. A. (2015). Surface acoustic wave amplification by direct current-voltage supplied to graphene film. *Applied Physics Letters*, *106*(2). https://doi.org/10.1063/1.4906033

Isensee, K., Kröger-Lui, N., & Petrich, W. (2018). Biomedical applications of mid-infrared quantum cascade lasers – a review. *Analyst*, *143*(24), 5888–5911. https://doi.org/10.1039/c8an01306c

Izquierdo-López, R., Fandan, R., Boscá, A., Calle, F., & Pedrós, J. (2023). Surface-acoustic-wave-driven graphene plasmonic sensor for fingerprinting ultrathin biolayers down to the monolayer limit. *Biosensors & Bioelectronics*, *237*, 115498. https://doi.org/10.1016/j.bios.2023.115498

Ju, L., Geng, B., Horng, J., Girit, C., Martin, M., Hao, Z., Bechtel, H. A., Liang, X., Zettl, A., Shen, Y. R., & Wang, F. (2011). *Nature Nanotechnoly*, *6*(10), 630–634.

Kamenetskii, E., Sadreev, A., & Miroshnichenko, A. (2018). *Fano resonances in optics and microwaves* (Vol. 219). Springer.

Kang, D.-H., Sun, H., Luo, M., Lu, K., Chen, M., Kim, Y., Jung, Y., Gao, X., Parluhutan, S. J., Ge, J., Koh, S. W., Giovanni, D., Sum, T. C., Wang, Q. J., Li, H., & Nam, D. (2021). Pseudo-magnetic field-induced slow carrier dynamics in periodically strained graphene. *Nature Communications*, *12*(1), 5087. https://doi.org/10.1038/s41467-021-25304-0

Katsnelson, M. I., Geim, A. K., & Novoselov, K. S. (2006). Chiral tunnelling and the klein paradox in graphene. *Nature physics*, *2*(9), 620–625. https://doi.org/10.1038/nphys384

Kazan, M., Pereira, S., Correia, M. R., & Masri, P. (2009). Directional dependence of aln intrinsic complex dielectric function, optical phonon lifetimes, and decay channels measured by polarized infrared reflectivity. *Journal of Applied Physics*, *106*(2), 023523–10. https://doi.org/10.1063/1.3177323

Kobayashi, Y., Tanaka, N., Okano, H., Takeuchi, K., Usuki, T., & Shibata, K. (1995). *Japanese Journal of Applied Physics*, *34*(5B), 2668–2673.

Kristament, C., Schwaighofer, A., Montemurro, M., & Lendl, B. (2018). A photothermal mach-zehnder interferometer for measuring caffeine and proteins in aqueous solutions using external cavity quantum cascade lasers. *10490*, 104900M–9. https://doi.org/10.1117/12.2290603

LaserScope by Block Engineering. (Last accessed 2024). https://www.blockeng.com/applications/lasers.html

Lavoie, H., Blaudez, D., Vaknin, D., Desbat, B., Ocko, B. M., & Salesse, C. (2002). Espectroscopic and structural properties of valine gramicidin a in monolayers at the air-water interface. *Biophysical Journal*, *83*(6), 3558–3569. https://doi.org/10.1016/S0006-3495(02)75356-3

Lean, E. G. (1973). III Interaction of Light and Acoustic Surface Waves. Elsevier Science & Technology. https://doi.org/10.1016/S0079-6638(08)70135-5

Lee, I.-H., Yoo, D., Avouris, P., Low, T., & Oh, S.-H. (2019). *Nature Nanotechnoly*, *14*, 313–319.

Levy, N., Burke, S. A., Meaker, K. L., Panlasigui, M., Zettl, A., Guinea, F., Neto, A. H. C., & Crommie, M. F. (2010). Strain-Induced Pseudo-Magnetic Fields Greater Than 300 Tesla in Graphene Nanobubbles. *Science*, *329*(5991), 544–547. https://doi.org/10.1126/science.1191700

Li, Y., Yan, H., Farmer, D. B., Meng, X., Zhu, W., Osgood, R. M., Heinz, T. F., & Avouris, P. (2014). Graphene plasmon enhanced vibrational sensing of surface-adsorbed layers. *Nano Letters*, *14*(3), 1573–1577. https://doi.org/10.1021/nl404824w

Lin, W.-W., Chen, I.-J., Cheng, T.-C., Tung, Y.-C., Chu, P.-Y., Chuang, C.-H., Hsieh, Y.-C., Huang, C.-C., Wang, Y.-T., Kao, C.-H., Roffler, S. R., & Cheng, T.-L. (2016). A secondary antibody-detecting molecular weight marker with mouse and rabbit igg fc linear epitopes for western blot analysis. *PloS One*, *11*(8), e0160418. https://doi.org/10.1371/journal.pone.0160418

Liu, N., Langguth, L., Weiss, T., Kästel, J., Fleischhauer, M., Pfau, T., & Giessen, H. (2009). Plasmonic analogue of electromagnetically induced transparency at the Drude damping limit. *Nature Materials*, *8*(9), 758–762. https://doi.org/10.1038/nmat2495

López-Lorente, Á. I., & Mizaikoff, B. (2016). Mid-infrared spectroscopy for protein analysis: Potential and challenges. *Analytical and Bioanalytical Chemistry*, *408*(11), 2875–2889. https://doi.org/10.1007/s00216-016-9375-5

Low, T., & Avouris, P. (2014). Graphene plasmonics for terahertz to mid-infrared applications. *ACS Nano*, *8*(2), 1086–1101. https://doi.org/10.1021/nn406627u

Lu, H., Tan, Y., McConville, J. P. V., Ahmadi, Z., Wang, B., Conroy, M., Moore, K., Bangert, U., Shield, J. E., Chen, L.-Q., Gregg, J. M., & Gruverman, A. (2019). Electrical Tunability of Domain Wall Conductivity in LiNbO3 Thin Films. *Advanced Materials*, *31*(48), e1902890–n/a. https://doi.org/10.1002/adma.201902890

Lucarini, V., Peiponen, K.-E., Saarinen, J. J., & Vartiainen, E. M. (2005). *Kramers-Kronig Relations in Optical Materials Research* (Vol. 110). Springer. https://doi.org/10.1007/b138913

Lüdeke, S., Pfeifer, M., & Fischer, P. (2011). Quantum-cascade laser-based vibrational circular dichroism. *Journal of the American Chemical Society*, *133*(15), 5704–5707. https://doi.org/10.1021/ja200539d

Maier, S. A. (2007). *Plasmonics: Fundamentals and Applications*. Springer US.

Masolin, A., Bouchard, P.-O., Martini, R., & Bernacki, M. (2013). Thermo-mechanical and fracture properties in single-crystal silicon. *Journal of Materials Science*, *48*(3), 979–988. https://doi.org/10.1007/s10853-012-6713-7

Mathews, S. A., Bingham, N. S., Suess, R. J., Charipar, K. M., Auyeung, R. C. Y., Kim, H., & Charipar, N. A. (2019). Thermally induced magnetic anisotropy in nickel films on surface acoustic wave devices. *IEEE Transactions on Magnetics*, *55*(2), 1–4. https://doi.org/10.1109/TMAG.2018.2860936

Matic, A., Baron, T., & Bassignot, F. (2017). Periodically poled LiNbO3 transducer on (YXl)/128° cut for RF applications, 214–217. https://doi.org/10.1109/FCS.2017.8088850

Matsuda, O., Tsutsui, K., Vaudel, G., Pezeril, T., Fujita, K., & Gusev, V. (2020). Optical generation and detection of gigahertz shear acoustic waves in solids assisted by a metallic diffraction grating. *Physical Review B*, *101*(22), 1. https://doi.org/10.1103/physrevb.101.224307

Mendelsohn, R., Mao, G., & Flach, C. R. (2010). Infrared reflection–absorption spectroscopy: Principles and applications to lipid–protein interaction in Langmuir films. *Biochimica et Biophysica Acta*, *1798*(4), 788–800. https://doi.org/10.1016/j.bbamem.2009.11.024

Metas VNA Tools. (Last accessed 2024). https://www.metas.ch/metas/en/home/fabe/hochfrequenz/vna-tools.html

Mirabella, F. M. (1985). Internal reflection spectroscopy. *Applied Spectroscopy Reviews*, *21*(1-2), 45–178. https://doi.org/10.1080/05704928508060428

MIRcat by Daylight Solutions. (Last accessed 2024). https://www.daylightsolutions.com/products/mircat/

Miseikis, V., Cunningham, J. E., Saeed, K., O'Rorke, R., & Davies, A. G. (2012). Acoustically induced current flow in graphene. *Applied Physics Letters*, *100*(13), 133105–4. https://doi.org/10.1063/1.3697403

Morgan, D. (2007). *Surface acoustic wave filters : With applications to electronic communications and signal processing* (2nd ed). Academic Press. https://doi.org/10.1016/B978-0-12-372537-0.X5000-6

Nafie, L. A., Keiderling, T. A., & Stephens, P. J. (1976). Vibrational circular dichroism. *Journal of the American Chemical Society*, *98*(10), 2715–2723. https://doi.org/10.1021/ja00426a007

Naumis, G. G., Barraza-Lopez, S., Oliva-Leyva, M., & Terrones, H. (2017). Electronic and optical properties of strained graphene and other strained 2D materials: a review. *Reports on Progress in Physics*, *80*(9), 096501. https://doi.org/10.1088/1361-6633/aa74ef

Neto, A. H. C., Guinea, F., Peres, N. M. R., Novoselov, K. S., & Geim, A. K. (2009). The electronic properties of graphene. *Reviews of Modern Physics*, *81*(1), 109–162. https://doi.org/10.1103/RevModPhys.81.109

Neuman, T., Huck, C., Vogt, J., Neubrech, F., Hillenbrand, R., Aizpurua, J., & Pucci, A. (2015). *Journal of Physical Chemistry C*, *119*(47), 26652–26662.

Novoselov, K. S., Geim, A. K., Morozov, S. V., Jiang, D., Katsnelson, M. I., Grigorieva, I. V., Dubonos, S. V., & Firsov, A. A. (2005). Two-dimensional gas of massless Dirac fermions in graphene. *Nature*, *438*(7065), 197–200. https://doi.org/10.1038/nature04233

Novoselov, K. S., Geim, A. K., Morozov, S. V., Jiang, D., Zhang, Y., Dubonos, S. V., Grigorieva, I. V., & Firsov, A. A. (2004). Electric field effect in atomically thin carbon films. *Science*, *306*(5696), 666–669. https://doi.org/10.1126/science.1102896

Novoselov, K. S., Jiang, Z., Zhang, Y., Morozov, S. V., Stormer, H. L., Zeitler, U., Maan, J. C., Boebinger, G. S., Kim, P., & Geim, A. K. (2007). Room-Temperature Quantum Hall Effect in Graphene. *Science*, *315*(5817), 1379. https://doi.org/10.1126/science.1137201

Oliva-Leyva, M., & Naumis, G. G. (2016). Sound waves induce Volkov-like states, band structure and collimation effect in graphene. *Journal of physics: Condensed matter*, *28*(2), 025301. https://doi.org/10.1088/0953-8984/28/2/025301

Ouhabaz, M., Belharet, D., Micard, Q., Costanza, M., Giuffrida, G., Bartasyte, A., Trigona, C., & Margueron, S. (2024). Microfabrication of piezoelectric MEMS based on thick LiNbO3 single-crystal films. *Nanotechnology*, *35*(18). https://doi.org/10.1088/1361-6528/ad1b00

Parmenter, R. H. (1953). The acousto-electric effect. *Physical Review*, *89*(5), 990–998. https://doi.org/10.1103/PhysRev.89.990

Preciado, E., Schülein, F. J. R., Nguyen, A. E., Barroso, D., Isarraraz, M., von Son, G., Lu, I.-H., Michailow, W., Möller, B., Klee, V., Mann, J., Wixforth, A., Bartels, L., & Krenner, H. J. (2015). Scalable fabrication of a hybrid field-effect and acousto-electric device by direct growth of monolayer MoS2/LiNbO3. *Nature Communications*, *6*(1), 8593. https://doi.org/10.1038/ncomms9593

Rasouli, H. R., Kaiser, D., Neumann, C., Frey, M., Eshaghi, G., Weimann, T., & Turchanin, A. (2023). Critical point drying of graphene field-effect transistors improves their electric transport characteristics. *Small Methods*, *7*(10), e2300288. https://doi.org/10.1002/smtd.202300288

Rayleigh, L. (1885). On waves propagated along the plane surface of an elastic solid. *Proceedings of the London Mathematical Society*, *s1-17*(1), 4–11. https://doi.org/10.1112/plms/s1-17.1.4

Rivelles, A., Yanes, R., Torres, L., Guedas, R., Izquierdo-López, R., Maicas, M., del Mar Sanz, M., Pedrós, J., Calle, F., López-Díaz, L., & Prieto, J. L. (2024). *Mechanism to transfer linear momentum from a surface acoustic wave to a magnetic domain wall*. https://arxiv.org/abs/2406.12778

Rodrigo, D., Limaj, O., Janner, D., Etezadi, D., de Abajo, F. J. G., Pruneri, V., & Altug, H. (2015). Mid-infrared plasmonic biosensing with graphene. *Science*, *349*(6244), 165–168. https://doi.org/10.1126/science.aab2051

Rodrigo, D., Tittl, A., Limaj, O., de Abajo, F. J. G., Pruneri, V., & Altug, H. (2017). Double-layer graphene for enhanced tunable infrared plasmonics. *Light, Science & Applications*, *6*(6), e16277. https://doi.org/10.1038/lsa.2016.277

Rotter, M., Wixforth, A., Ruile, W., Bernklau, D., & Riechert, H. (1998). Giant acoustoelectric effect in GaAs/LiNbO3 hybrids. *Applied Physics Letters*, *73*(15), 2128–2130. https://doi.org/10.1063/1.122400

Ruppert, C., Neumann, J., Kinzel, J. B., Krenner, H. J., Wixforth, A., & Betz, M. (2010). Surface acoustic wave mediated coupling of free-space radiation into surface plasmon polaritons on plain metal films. *Physical Review B: Condensed Matter and Materials Physics*, *82*(8). https://doi.org/10.1103/PhysRevB.82.081416

Sacher Lasertechnik. (Last accessed 2024). https://www.sacher-laser.com/home/scientific-lasers/quantum_cascade_laser.html

Saleh, B. E. A., & Teich, M. C. (2019). *Fundamentals of photonics* (3rd ed). Wiley.

Santos, P. V., Schumann, T., Oliveira, M. H., Lopes, J. M. J., & Riechert, H. (2013). Acousto-electric transport in epitaxial monolayer graphene on SiC. *Applied Physics Letters*, *102*(22). https://doi.org/10.1063/1.4809726

Sarma, S. D., Adam, S., Hwang, E. H., & Rossi, E. (2011). Electronic transport in two-dimensional graphene. *Reviews of Modern Physics*, *83*(2), 407–470. https://doi.org/10.1103/revmodphys.83.407

Schiefele, J., Pedrós, J., Sols, F., Calle, F., & Guinea, F. (2013). Coupling light into graphene plasmons through surface acoustic waves. *Physical Review Letters*, *111*(23), 237405. https://doi.org/10.1103/PhysRevLett.111.237405

Schwaighofer, A., Montemurro, M., Freitag, S., Kristament, C., Culzoni, M. J., & Lendl, B. (2018). Beyond fourier transform infrared spectroscopy: External cavity quantum cascade laser-based mid-infrared transmission spectroscopy of proteins in the amide i and amide ii region. *Analytical Chemistry*, *90*(11), 7072–7079. https://doi.org/10.1021/acs.analchem.8b01632

Sela, E., Bloch, Y., von Oppen, F., & Shalom, M. B. (2020). Quantum Hall Response to Time-Dependent Strain Gradients in Graphene. *Physical Review Letters*, *124*(2), 026602. https://doi.org/10.1103/PhysRevLett.124.026602

Shilton, J. M., Mace, D. R., Talyanskii, V. I., Simmons, M. Y., Pepper, M., Churchill, A. C., & Ritchie, D. A. (1995). Experimental study of the acoustoelectric effects in GaAs-AlGaAs heterostructures. *Journal of Physics: Condensed Matter*, *7*(39), 7675–7685. https://doi.org/10.1088/0953-8984/7/39/010

Simon, S. H. (1996). Coupling of surface acoustic waves to a two-dimensional electron gas. *Physical Review B*, *54*(19), 13878–13884. https://doi.org/10.1103/physrevb.54.13878

Smith, R. J., Li, W., Coulson, J., Clark, M., Somekh, M. G., & Sharples, S. D. (2014). Spatially resolved acoustic spectroscopy for rapid imaging of material microstructure and grain orientation. *Measurement Science and Technology*, *25*(5), 55902. https://doi.org/10.1088/0957-0233/25/5/055902

Spero IR by Daylight Solutions. (Last accessed 2024). https://www.daylightsolutions.com/products/spero/

Sun, X., Shiokawa, S., & Matsui, Y. (1991). Interactions of surface plasmons with surface acoustic waves and the study of the properties of Ag films. *Journal of Applied Physics*, *69*(1), 362–366. https://doi.org/10.1063/1.347722

Tyagi, A., Mišeikis, V., Martini, L., Forti, S., Mishra, N., Gebeyehu, Z. M., Giambra, M. A., Zribi, J., Frégnaux, M., Aureau, D., Romagnoli, M., Beltram, F., & Coletti, C. (2022). Ultra-clean high-mobility graphene on technologically relevant substrates. *Nanoscale*, *14*(6), 2167–2176. https://doi.org/10.1039/D1NR05904A

Vigo Photonics Catalog 2020/21. (2021). https://vigo.com.pl/wp-content/uploads/2021/03/VIGO_katalog_2020-2021-LQ.pdf

Vigo Photonics: Immersion Lenses Technology. (Last accessed 2024). https://vigophotonics.com/articles/immersion-lenses-technology/

Vogt, J., Huck, C., Neubrech, F., Toma, A., Gerbert, D., & Pucci, A. (2015). Impact of the plasmonic near- and far-field resonance-energy shift on the enhancement of infrared vibrational signals. *Physical Chemistry Chemical Physics*, *17*(33), 21169–21175. https://doi.org/10.1039/C4CP04851B

Voltmer, F. W., & White, R. M. (1965). Direct piezoelectric coupling to surface elastic waves. *Applied Physics Letters*, *7*, 314–316. https://doi.org/10.1063/1.1754276

Vozmediano, M., Katsnelson, M., & Guinea, F. (2010). Gauge fields in graphene. *Physics Reports*, *496*(4), 109–148. https://doi.org/10.1016/j.physrep.2010.07.003

Vukovic, N., Segués, A., Huang, S., Waterfall, M., Sijts, A. J. A. M., & Zaiss, D. M. (2023). Mouse IgG2a Isotype Therapeutic Antibodies Elicit Superior Tumor Growth Control Compared with mIgG1 or mIgE. *Cancer Research Communications*, *3*(1), 109–118. https://doi.org/10.1158/2767-9764.CRC-22-0356

Wang, F., & Shen, Y. R. (2006). General properties of local plasmons in metal nanostructures. *Physical Review Letters*, *97*(20), 206806. https://doi.org/10.1103/PhysRevLett.97.206806

Wixforth, A. (2003). Acoustically driven planar microfluidics. *Superlattices and Microstructures*, *33*(5), 389–396. https://doi.org/10.1016/j.spmi.2004.02.015

Yamanouchi, K., & Furuyashiki, H. (1984). New low-loss SAW filter using internal floating electrode reflection types of single-phase unidirectional transducer. *Electronics Letters*, *20*(24), 989–990. https://doi.org/10.1049/el:19840672

Yan, H., Low, T., Zhu, W., Wu, Y., Freitag, M., Li, X., Guinea, F., Avouris, P., & Xia, F. (2013). Damping pathways of mid-infrared plasmons in graphene nanostructures. *Nature Photonics*, *7*(5), 394–399. https://doi.org/10.1038/nphoton.2013.57

Yeh, N. C., Teague, M. L., Yeom, S., Standley, B. L., Wu, R. T. P., Boyd, D. A., & Bockrath, M. W. (2011). Strain-induced pseudo-magnetic fields and charging effects on CVD-grown graphene. *Surface Science*, *605*(17), 1649–1656. https://doi.org/10.1016/j.susc.2011.03.025

Yi, J., You, E.-M., Ding, S.-Y., & Tian, Z.-Q. (2020). Unveiling the molecule–plasmon interactions in surface-enhanced infrared absorption spectroscopy. *National Science Review*, *7*(7), 1228–1238. https://doi.org/10.1093/nsr/nwaa054

Zhai, F., Zhao, X., Chang, K., & Xu, H. Q. (2010). Magnetic barrier on strained graphene: A possible valley filter. *Physical Review B*, *82*(11). https://doi.org/10.1103/physrevb.82.115442

Zhan, T., Shi, X., Dai, Y., Liu, X., & Zi, J. (2013). Transfer matrix method for optics in graphene layers. *Journal of Physics: Condensed Matter*, *25*(21), 215301. https://doi.org/10.1088/0953-8984/25/21/215301

Zhang, N., Luo, W., Wang, L., Fan, J., Wu, W., Ren, M., Zhang, X., Cai, W., & Xu, J. (2022). Strong in-plane scattering of acoustic graphene plasmons by surface atomic steps. *Nature Communications*, *13*, 983. https://doi.org/10.1038/s41467-022-28614-z

Zhao, P., Sharma, C. H., Liang, R., Glasenapp, C., Mourokh, L., Kovalev, V. M., Huber, P., Prada, M., Tiemann, L., & Blick, R. H. (2022). Acoustically Induced Giant Synthetic Hall Voltages in Graphene. *Physical Review Letters*, *128*(7), 256601. https://doi.org/10.1103/PhysRevLett.128.256601

Zhao, Y., Hu, X., Chen, G., Zhang, X., Tan, Z., Chen, J., Ruoff, R. S., Zhu, Y., & Lu, Y. (2013). Infrared biosensors based on graphene plasmonics: Modeling. *Physical Chemistry Chemical Physics*, *15*(40), 17118–17125. https://doi.org/10.1039/c3cp51952j

Zurich Instruments Toolkit. (Last accessed 2024). https://github.com/zhinst/zhinst-toolkit?tab=readme-ov-file

ZurichInstruments. (2023). *Principles of lock-in detection and the state of the art* (tech. rep.). https://www.zhinst.com/sites/default/files/documents/2023-04/zi_whitepaper_principles_of_lock-in_detection_0.pdf

Appendix A

COM parameters

Table A.1 displays the values of the COM fitting parameters from the calculations presented in Chapter 4.

Analyte	ω_{res} (cm^{-1})	d (nm)	κ (cm^{-1})	F_1 (cm^{-1})	F_2 (cm^{-1})
CBP	1479	0	0	36.4	0
	1479	0.35	2.32	37.7	5.06
	1479	1	3.81	32.7	7.0
	1479	2	5.36	26.4	6.78
A/G-IgG	1530	0	0	3.07	0
	1530	8 (bilayer)	29.3	0.98	0.41
	1655	0	0	5.00	0
	1655	8 (bilayer)	48.0	1.04	0.50
VGA	1452	0	0	4.73	0
	1452	2.5 (monolayer)	11.2	3.29	0.81
	1452	5	15.6	2.47	0.79
	1452	7.5	18.8	1.93	0.68

Table A.1: COM fitting parameters.

Appendix B

List of contributions

B.1 Journal Articles

- **R. Izquierdo-López**, R. Fandan, A. Boscá, F. Calle & J. Pedrós. Surface-acoustic wave-driven graphene plasmonic sensor for fingerprinting ultrathin biolayers down to the monolayer limit. *Biosensors & Bioelectronics* **237**, 115498 (2023).
- A. Rivelles, R. Yanes, L. Torres, R. Guedas, **R. Izquierdo-López**, M. Maicas, M. del Mar Sanz, J. Pedrós, F. Calle, L. López-Díaz, & J.L. Prieto. Mechanism to transfer linear momentum from a surface acoustic wave to a magnetic domain wall. https://arxiv.org/abs/2406.12778 (2024).

B.2 Conferences

- **R. Izquierdo-López**, J. Pedrós, R. Fandan, A. Boscá & F. Calle. SAW-driven plasmons in graphene heterostructures for sensing ultrathin layers. *Graphene 2020.*
- **R. Izquierdo-López**, J. Pedrós, R. Fandan, A. Boscá & F. Calle. SAW-driven plasmons in graphene heterostructures for fingerprinting ultrathin polymer layers. *Spanish Conference on Electron Devices CDE 2021.*
- J. Pedrós, R. Fandan, A. Boscá, **R. Izquierdo-López** & F. Calle. Surface acoustic waves in graphene & 2D materials for manipulating light-matter interactions. *NanoSpain 2022.*
- S. Guellati, R. Fandan, **R. Izquierdo-López**, A. Boscá, F. Calle & J. Pedrós. High Q factor two-port SAW resonators with single- & multi-cavity modes. *Spanish Conference on Electron Devices CDE 2023.*
- J. Pedrós, R. Fandan, **R. Izquierdo-López**, A. Boscá & F. Calle. Dynamic Control of Light-Matter Interactions in Graphene & 2D Crystals by Surface Acoustic Waves. *NanoSeries 2023.*
- **R. Izquierdo-López**, R. Fandan, A. Boscá, F. Calle & J. Pedrós. Surface-acoustic-

wave-driven graphene plasmonic sensor for fingerprinting ultrathin biolayers. *Graphene 2023.*

- R. Fandan, **R. Izquierdo-López**, A. Boscá, F. Calle & J. Pedrós. Graphene & 2D crystal polaritonics enabled by surface acoustic waves. *Conference of Advanced Materials in Spain AMatS 2023.*
- A. Rivelles, R. Guedas, R. Yanes, L. Torres, **R. Izquierdo-López**, M. C. Maicas, M. Sanz, J. Pedrós, F. Calle, J. Prieto and L. Lopez-Diaz. Control of the Moving Direction of Magnetic Domain Walls by Surface Acoustic Waves. *IEEE International Magnetics Conference, INTERMAG 2024*
- **R. Izquierdo-López**, R. Fandan, A. Boscá, F. Calle & J. Pedrós. SAW-driven graphene plasmonic biosensor for fingerprinting ultrathin layers. *Conference of Advanced Materials in Spain AMatS 2024.*